

Computing the quasipotential for highly dissipative and chaotic SDEs. An application to stochastic Lorenz'63.

Maria Cameron^{*1} and Shuo Yang^{†1}

¹Department of Mathematics, University of Maryland, College Park, MD 20742, USA

June 18, 2019

Abstract

The study of noise-driven transitions occurring rarely on the time-scale of systems modeled by SDEs is of crucial importance for understanding such phenomena as genetic switches in living organisms and magnetization switches of the Earth. For a gradient SDE, the predictions for transition times and paths between its metastable states are done using the potential function. For a nongradient SDE, one needs to decompose its forcing into a gradient of the so-called quasipotential and a rotational component, which cannot be done analytically in general.

We propose a methodology for computing the quasipotential for highly dissipative and chaotic systems built on the example of Lorenz'63 with an added stochastic term. It is based on the ordered line integral method, a Dijkstra-like quasipotential solver, and combines 3D computations in whole regions, a dimensional reduction technique, and 2D computations on radial meshes on manifolds or their unions. Our collection of source codes is available on M. Cameron's web page and on GitHub.

1 Introduction

Suppose a system is evolving according to a stochastic differential equation (SDE) of the form

$$d\mathbf{x} = \mathbf{b}(\mathbf{x})dt + \sqrt{\epsilon}d\mathbf{w}, \quad \mathbf{x} \in \mathbb{R}^d, \quad (1)$$

where $\mathbf{b}(\mathbf{x})$ is a continuously differentiable vector field, $d\mathbf{w}$ is the standard Brownian motion, and ϵ is a small parameter. The quasipotential is a key function of the large deviation theory (LDT) [15] that allows one to find a collection of useful asymptotic estimates for long-time dynamics of such systems. They include the invariant probability measure, expected escape times from neighborhoods of attractors of the corresponding ODE $\dot{\mathbf{x}} = \mathbf{b}(\mathbf{x})$ lying within their basins, and maximum likelihood escape paths from the basins. The quasipotential can be viewed as an analogue to the potential function $V(\mathbf{x})$, $\mathbf{x} \in \mathbb{R}^d$, for a gradient SDE with deterministic term $-\nabla V(\mathbf{x})$. The quasipotential is defined as the solution to the Freidlin-Wentzell action functional minimization problem. The quasipotential is Lipschitz-continuous in any bounded domain but not necessarily continuously differentiable [4]. Unfortunately, it can be found analytically only in special cases, for example, for linear SDEs [8, 9].

*cameron@math.umd.edu

†shuoyang@math.umd.edu

Ordered line integral methods (OLIMs) for computing the quasipotential for SDEs of the form (1) in whole regions on regular rectangular meshes were introduced in [11] for 2D and extended to 3D in [38]. They are Dijkstra-like solvers that advance the solution from mesh points with smaller values to those with larger values¹ without iteration. Their general structure is inherited from the ordered upwind method (OUM) [28, 29], but there are important differences. First, unlike the OUM that uses the upwind finite difference scheme, the OLIMs solve a local functional minimization problem at every step approximating a segment of curve with a segment of straight line, and the integral along it by an at least second order accurate quadrature rule. This renders their observed rate of convergence superlinear for some cases, and reduces error constants by two to three orders of magnitude in comparison with the OUM. Second, while the OUM is practical only for 2D problems due to large CPU times in larger dimensions, the OLIMs have been successfully extended for 3D. This became possible due to the hierarchical update strategy [11, 38], the use of the Karush-Kuhn-Tucker optimality conditions to eliminate unnecessary updates, and a number of implementational rationalizations.

In previous works [11, 12, 38], the OLIMs were developed for computing the quasipotential for mild-to-moderate ratio $\Xi(\mathbf{x})$ of the magnitudes of the rotational and potential components of the vector field $\mathbf{b}(\mathbf{x})$ in (1). In all test problems considered in [11, 12, 38], $\Xi(\mathbf{x})$ did not exceed 10 within the important region around the attractor with respect to which the quasipotential was computed. For all these test problems, the black-box algorithms [11, 12, 38] produced numerical solutions with small relative errors.

Unfortunately, if one applies the black-box `olim3D` quasipotential solver from [38] to a highly dissipative and chaotic system such as Lorenz'63 with an added small white noise, the relative error of the numerical solution might be large leading to completely wrong estimates for escape rates. For the parameter values $\sigma = 10$, $\beta = 8/3$, and $\rho \gtrsim 15$, the quasipotential computed with respect to one of the point attractors will become progressively inaccurate as ρ increases. We show in this work that, as ρ approaches $\rho_2 \approx 24.74$ (where a subcritical Hopf bifurcation happens), the upper bound for the ratio $\Xi(\mathbf{x})$ blows up at any point of the computational domain of interest. Even if one uses a very good desktop computer², this problem cannot be cured by mesh refinement due to the limited computer's memory: the size of a 3D mesh cannot exceed 1000^3 by much.

In this work, we propose an approach for computing the quasipotential, finding maximum likelihood transition paths, and estimating escape times from basins of attractors for highly dissipative and possibly chaotic systems perturbed by small white noise. This approach is suitable for systems where the 3D dynamics, after some short transition time, takes place in a small neighborhood of a 2D manifold or a union of 2D manifolds consisting of certain characteristics of the corresponding ODE (see Assumption 1 in Section 4.2 below). Whether or not this phenomenon takes place can be identified from the plots of the 3D level sets of the computed quasipotential. We develop a technique for extracting these manifolds and generating so-called radial meshes on them. We adjust and test the OLIM for 2D radial meshes and compute the quasipotential on the constructed 2D manifolds or their unions.

The proposed techniques have been developed on the stochastic Lorenz'63:

$$d\mathbf{x} = \begin{bmatrix} \sigma(x_2 - x_1) \\ x_1(\rho - x_3) - x_2 \\ x_1x_2 - \beta x_3 \end{bmatrix} dt + \sqrt{\epsilon}d\mathbf{w}, \quad \text{where } \mathbf{x} \equiv \begin{bmatrix} x_1 \\ x_2 \\ x_3 \end{bmatrix}, \quad (2)$$

¹This is only approximately true. See Ref. [29] for details.

²We use iMac 2017 with processor 4.2 GHz Intel Core i7 and memory 64 GB 2400 MHz DDR4.

with $\sigma = 10$, $\beta = 8/3$, and $0.5 \leq \rho < \rho_2 \approx 24.74$. To the best of our knowledge, this is the first time when the quasipotential is computed for a chaotic 3D system in the whole region and 3D computations are refined by 2D computations on certain manifolds. We study transitions between the stable equilibria at $\rho = 12, 15$, and 20 , and between the stable equilibria and the strange attractor at $\rho = 24.4$, and find a collection of quasipotential barriers for them. Our transition paths obtained by a direct integration using the computed quasipotential can be compared to those found in [40] using the minimum action method, a path-based method consisting in a direct minimization of the Freidlin-Wentzell action in the path-space. At $\rho = 24.4$, we compare two plausible transition mechanisms from the strange attractor to the equilibria. We offer a number of plots of 3D level sets of the quasipotential at various values of ρ varying from 0.5 to 24.4 and supplement them with links to youtube videos for a better 3D visualization. For $\rho \geq 15$, when 2D approximation becomes accurate enough, we perform refined 2D computations of the quasipotential.

Aiming at making our results readily reproducible, we made most of the codes developed for this project publicly available at M. Cameron’s web page [5] – see the package `Qpot4lorenz63.zip`, and on GitHub [6]. All codes mentioned throughout this paper are included in this package. A user guide for the codes is also provided there.

The techniques developed in this work can be used for analysis of other stochastic systems. For example, the computation of the quasipotential for the 3D genetic switch model from [23] would benefit from performing a refined 2D computation on a radial mesh on a 2D manifold as suggested by Fig. 9 in [38]. Gissinger’s 3D model [16] relevant for the reversals of the magnetic field of the Earth can be analyzed using the tools developed in this work.

The rest of the paper is organized as follows. In Section 2, some necessary background on the quasipotential is given. A brief overview of the dynamics of Lorenz’63 at $\sigma = 10$, $\beta = 8/3$, and $0 < \rho < \infty$ is offered in Section 3 and Appendix B. Numerical techniques for computing the quasipotential are described in Section 4. The application to stochastic Lorenz’63 is presented in Section 5. We summarize our findings in Section 6. Some technical details are explained in Appendices A–G.

2 Definition and significance of the quasipotential

To explain what is the quasipotential [15], we first assume that the vector field $\mathbf{b}(\mathbf{x})$ in SDE (1) admits the following smooth orthogonal decomposition:

$$\mathbf{b}(\mathbf{x}) = -\frac{1}{2}\nabla u(\mathbf{x}) + \mathbf{l}(\mathbf{x}), \quad \nabla u(\mathbf{x}) \cdot \mathbf{l}(\mathbf{x}) = 0. \quad (3)$$

If $\mathbf{l}(\mathbf{x}) \equiv \mathbf{0}$, i.e., if the field $\mathbf{b}(\mathbf{x})$ were gradient, the Gibbs measure

$$\mu(\mathbf{x}) = Z^{-1}e^{-u(\mathbf{x})/\epsilon} \quad (4)$$

would be the invariant probability density for SDE (1). Suppose $\mathbf{l}(\mathbf{x})$ is not identically zero. Plugging the Gibbs measure (4) into the stationary Fokker-Planck equation for SDE (1)

$$\frac{1}{2}\Delta\mu(\mathbf{x}) - \nabla \cdot (\mu(\mathbf{x})\mathbf{b}(\mathbf{x})) = 0 \quad (5)$$

we find that it is invariant if and only if $\mathbf{l}(\mathbf{x})$ is divergence-free, i.e., $\nabla \cdot \mathbf{l}(\mathbf{x}) \equiv 0$. In this case, the function $u(\mathbf{x})$ would play the role of a potential.

Unfortunately, the orthogonal decomposition (3) where $\mathbf{l}(\mathbf{x})$ is divergence-free does not typically exist. However, a function $U(\mathbf{x})$ called the quasipotential that gives asymptotic estimates for the invariant probability measure near attractors of $\dot{\mathbf{x}} = \mathbf{b}(\mathbf{x})$ in the limit $\epsilon \rightarrow 0$ can be designed [15].

Suppose that the vector field $\mathbf{b}(\mathbf{x})$ is continuously differentiable. In addition, we assume that the ODE

$$\dot{\mathbf{x}} = \mathbf{b}(\mathbf{x}) \quad (6)$$

has a finite number of attractors, and every trajectory of (6) remains in a bounded region as $t \rightarrow \infty$. Let A be an attractor of (6). The quasipotential with respect to A is defined as the solution of the minimization problem

$$U(\mathbf{x}) = \inf_{\phi, T_0, T_1} \{S_{T_0, T_1}(\phi) \mid \phi(T_0) \in A, \phi(T_1) = \mathbf{x}\}, \quad (7)$$

where the infimum of the Freidlin-Wentzell action

$$S_{T_0, T_1}(\phi) = \frac{1}{2} \int_{T_0}^{T_1} \|\dot{\phi} - \mathbf{b}(\phi)\|^2 dt \quad (8)$$

is taken over the set of absolutely continuous paths ϕ with endpoints at A and \mathbf{x} , and all times $T_0, T_1 \in \mathbb{R}$. The infimum with respect to T_0 and T_1 can be taken analytically [15, 19, 20] resulting in the geometric action (see Appendix A)

$$S(\psi) = \int_0^L (\|\psi'\| \|\mathbf{b}(\psi)\| - \psi' \cdot \mathbf{b}(\psi)) ds, \quad (9)$$

where the path ψ is parametrized by its arclength, and L is the length of ψ . As a result, the definition of the quasipotential can be rewritten in terms of the geometric action:

$$U(\mathbf{x}) = \inf_{\psi} \{S(\psi) \mid \psi(0) \in A, \psi(L) = \mathbf{x}\}. \quad (10)$$

We have been using definition (10) to develop quasipotential solvers.

Using Bellman's principle of optimality [2], one can show [4] that the quasipotential $U(\mathbf{x})$ satisfies the Hamilton-Jacobi equation (see Appendix A)

$$\frac{1}{2} \|\nabla U(\mathbf{x})\|^2 + \mathbf{b}(\mathbf{x}) \cdot \nabla U(\mathbf{x}) = 0, \quad U(A) = 0. \quad (11)$$

Eq. (11) implies that

$$\mathbf{b}(\mathbf{x}) = -\frac{1}{2} \nabla U(\mathbf{x}) + \mathbf{l}(\mathbf{x}), \quad \text{where } \mathbf{l}(\mathbf{x}) := \mathbf{b}(\mathbf{x}) + \frac{1}{2} \nabla U(\mathbf{x}) \text{ is orthogonal to } \nabla U(\mathbf{x}). \quad (12)$$

We will refer to $-(1/2)\nabla U(\mathbf{x})$ and $\mathbf{l}(\mathbf{x})$ as the potential and rotational components respectively.

We remark that the boundary value problem (BVP) (11) is ill-posed. It always has the trivial solution identically equal to zero and may or may not have a smooth nontrivial solution. The quasipotential defined by (7) or (10) is a viscosity solution¹ to (11) [10]. The other complication is that even a nontrivial solution to this BVP, classical or viscosity, may not be unique due to the fact that the boundary condition is imposed on an attractor [21]. For example, if $\mathbf{b}(\mathbf{x}) = B\mathbf{x}$ where B is

¹A viscosity solution to a first-order nonlinear PDE $f(\mathbf{x}, u, \nabla u) = 0$ is a continuous but possibly nondifferentiable function obtained as the limit of a sequence of smooth solutions to $f(\mathbf{x}, u, \nabla u) = \epsilon \Delta u$ as $\epsilon \rightarrow \infty$.

a matrix with all eigenvalues having negative real parts, the number of solutions of (11) with the BC $u(\mathbf{0}) = 0$ is equal to the number of invariant subspaces for B .

Nonetheless, (11) is instrumental in deriving the equation for *minimum action paths* (MAPs) a.k.a. *maximum likelihood paths* or *instantons* that minimize the geometric action (9) [15, 4] (see Appendix A):

$$\psi'(s) = \frac{\mathbf{b}(\psi(s)) + \nabla U(\psi(s))}{\|\mathbf{b}(\psi(s)) + \nabla U(\psi(s))\|}. \quad (13)$$

Once the quasipotential is computed, one can shoot a MAP from a given point \mathbf{x} back to the attractor A by integrating (13) backward in s . Alternatively, MAPs can be found by path-based methods [14, 39, 19, 20] that directly minimize the Freidlin-Wentzell action or the geometric action.

The mentioned asymptotic estimate for the invariant probability density within a level set of the quasipotential completely lying in the basin $\mathcal{B}(A)$ of A is [15]

$$\mu(\mathbf{x}) \asymp e^{-U(\mathbf{x})/\epsilon}, \quad \text{i.e.} \quad \lim_{\epsilon \rightarrow 0} (-\epsilon \log \mu(\mathbf{x})) = U(\mathbf{x}). \quad (14)$$

The symbol \asymp denotes the logarithmic equivalence clarified in (14). The expected escape time from $\mathcal{B}(A)$ can also be estimated up to exponential order [15]:

$$\mathbb{E}[\tau_{\mathcal{B}(A)}] \asymp e^{U(\mathbf{x}^*)/\epsilon}, \quad \text{where} \quad U(\mathbf{x}^*) = \min_{\mathbf{x} \in \partial\mathcal{B}(A)} U(\mathbf{x}). \quad (15)$$

In some common special cases, a sharp estimate for the expected escape time can be obtained [3].

The term *transition state* is often encountered in chemical physics literature. Mostly it refers to a saddle lying on the manifold separating two basins of attraction. The dynamics of the Lorenz system are complicated, and basins of its attractors are tightly interlaced for $\rho \gtrsim 20$. To accommodate such situations, we will define the term *escape state*.

Definition 2.1. *Consider a system evolving according to SDE (1). Let A be an attractor of the corresponding ODE (6). The escape state from A is the set of points minimizing the quasipotential with respect to A over the boundary of the basin of A .*

The quasipotential at the escape state of A defines the expected escape time from the basin of A up to exponential order according to Eq. (15).

3 A brief overview of Lorenz'63

The Lorenz'63 system

$$\begin{aligned} \dot{x}_1 &= \sigma(x_2 - x_1), \\ \dot{x}_2 &= x_1(\rho - x_3) - x_2, \\ \dot{x}_3 &= x_1x_2 - \beta x_3 \end{aligned} \quad (16)$$

is one of the most fascinating and transformative ODE models proposed in the twentieth century. E. Lorenz [24] derived it from Saltzman's 2D cellular convection model [27] using a Fourier expansion and truncating the trigonometric series to include a total of three terms. He proved that the resulting system exhibits a new type of long-term behavior. All trajectories of (16) stay in a bounded region. For $\sigma = 10$, $\beta = 8/3$, and $\rho = 28$, their ω -limit sets form an "infinite complex of surfaces", i.e., a fractal, whose Hausdorff dimension is 2.06 [35], later named the Lorenz attractor. The Lorenz map

[24], a 1D map $z_{n+1} = f(z_n)$, where z_n is the n th maximum of the z -component of a trajectory, and f is the function estimated numerically, explained the divergence of arbitrarily close characteristics. It has become instrumental for analysis of chaotic dynamical systems.

The study of the Lorenz'63 system bursted in mid-1970s, perhaps due to the progress in the computer industry. A number of remarkable properties and quantitative characteristics have been discovered. The topological structure of the Lorenz attractor was studied in [17, 26, 36]. The phenomenon called preturbulence was described in [22]. The value $\rho_1 \approx 24.06$ at which the Lorenz attractor is born for $\sigma = 10$ and $\beta = 8/3$ was found in [37] using a functional fit to the Lorenz map. Homoclinic explosions, period-doubling cascades, and periodicity windows were investigated in [31]. A beautiful overview of the Lorenz system is given in [33] (Chapters 9–12). Nowadays, the Lorenz system is a popular test model for new methods in such fields as machine learning and forecasting (e.g. [13, 30, 18]).

It is easy to check that (16) is invariant under the symmetry transformation $(x_1, x_2, x_3) \mapsto (-x_1, -x_2, x_3)$. We fix the parameters $\sigma = 10$ and $\beta = 8/3$ and consider the dynamics of (16) as ρ grows from zero to infinity. The notation and bifurcations important for the further presentation are summarized in Table 1. A more detailed description of the dynamics of (16) for $0 < \rho < \infty$ is given in Appendix B.

Table 1: A summary of bifurcations and notation for Lorenz'63 (16) for $\sigma = 10$, $\beta = 8/3$, and $0 < \rho \leq \rho_2 \approx 24.74$.

Range of ρ	Comments & notation
$0 < \rho < 1$	The origin is the unique globally attracting equilibrium.
$\rho = 1$	Supercritical pitchfork bifurcation.
$1 < \rho < \rho_0 \approx 13.926$	The origin is a Morse index one saddle for $1 < \rho < \infty$. Equilibria C_{\pm} are located at $C_{\pm} = \left(\pm\sqrt{\beta(\rho - 1)}, \pm\sqrt{\beta(\rho - 1)}, \rho - 1 \right)$. C_{\pm} are asymptotically stable for $1 < \rho < \rho_2$.
$\rho = \rho_0 \approx 13.926$	Homoclinic orbits starting and ending at the origin exist.
$\rho_0 < \rho < \rho_1 \approx 24.06$	C_{\pm} are surrounded by saddle cycles γ_{\pm} respectively. Chaotic dynamics (“preturbulence”) is developing as ρ grows. We introduce cones Υ_{\pm} with vertices at C_{\pm} and passing through γ_{\pm} respectively: $\Upsilon_+ := \{C_+ + t(\mathbf{x} - C_+) \mid t \geq 0, \mathbf{x} \in \gamma_+\}$.
$\rho = \rho_1 \approx 24.06$	The birth of the Lorenz attractor A_L (a strange attractor).
$\rho_1 < \rho < \rho_2 \approx 24.74$	A_L coexists with asymptotically stable equilibria C_{\pm} .
$\rho = \rho_2 \approx 24.74$	A subcritical Hopf bifurcation: γ_{\pm} shrink to C_{\pm} respectively.

In this work, we consider the Lorenz system perturbed by small white noise (2). The noise term regularizes the chaotic deterministic dynamics of (16) in the sense that one can predict the future probability density function given the current one by solving the Fokker-Planck equation. On the other hand, the presence of the noise term enables escapes from any neighborhood of an attractor of (16). If ρ is such that there are multiple attractors, noise-induced transitions between their neighborhoods become possible.

4 Numerical methods

In this section, we describe numerical techniques developed for computing the quasipotential for highly dissipative and chaotic systems where the ratio of the magnitudes of the rotational and potential components is of the order of 10^3 .

4.1 A brief overview of ordered line integral methods (OLIMs)

We start with a brief overview the OLIMs. A comprehensive description of the implementation of the OLIM in 3D is provided in [38]. It involves many technical details that are important for making the solver fast. A C source code `olim3D4Lorenz63.c` set up to compute the quasipotential for (2) and an instruction on how to run are available in [5, 6].

The OLIMs belong to the family of label-setting algorithms [7] and inherit their set of labels from the OUM [28, 29]. Labels of mesh points indicate their statuses. A mesh point is **Accepted** if the value of the computed function (the quasipotential in our case) is finalized at it and all its nearest neighbors also have finalized values. **Accepted** points are not used for updating values at other mesh points. A mesh point is **Accepted Front** if the value at it is finalized but it has at least one nearest neighbor with a non-finalized value. **Considered** mesh points are those with non-finalized tentative values that have at least one **Accepted Front** nearest neighbor. **Unknown** mesh points have no **Accepted Front** nearest neighbors and the values at them have not been proposed yet.

The OLIMs use several kinds of neighborhoods of mesh points. The neighborhoods are defined via distances between indices of the mesh points. Let $\mathbf{p} := (i, j, k) \in \mathbb{Z}^3$ and $\mathbf{p}_0 := (i_0, j_0, k_0) \in \mathbb{Z}^3$ be the lattice points corresponding to the mesh points \mathbf{x} and \mathbf{x}_0 respectively. In other words, \mathbf{p} and \mathbf{p}_0 are the indices of the mesh points \mathbf{x} and \mathbf{x}_0 , respectively. Recall that the l_q , $q = 1, 2$, and l_∞ distances between \mathbf{p} and \mathbf{p}_0 are defined as

$$\begin{aligned} \|\mathbf{p} - \mathbf{p}_0\|_q &:= [|i - i_0|^q + |j - j_0|^q + |k - k_0|^q]^{1/q} \quad \text{and} \\ \|\mathbf{p} - \mathbf{p}_0\|_\infty &:= \max\{|i - i_0|, |j - j_0|, |k - k_0|\}, \end{aligned}$$

respectively. Let \mathcal{I} be the set of indices of all mesh points.

- The near neighborhood typically containing 26 points

$$\mathcal{N}_{\text{near}}(\mathbf{p}_0) := \{\mathbf{p} \in \mathcal{I} \mid \|\mathbf{p} - \mathbf{p}_0\|_1 \leq 3 \text{ and } \|\mathbf{p} - \mathbf{p}_0\|_\infty = 1\}$$

is used for recruiting **Unknown** points to **Considered** and changing the status of **Accepted Front** points to **Accepted**. Correspondingly, the near neighborhood of the mesh point \mathbf{x}_0 is defined as

$$\mathcal{N}_{\text{near}}(\mathbf{x}_0) := \{\mathbf{x} \mid \mathbf{p} \in \mathcal{N}_{\text{near}}(\mathbf{p}_0)\}.$$

- The far neighborhood $\mathcal{N}_{\text{far}}^K(\mathbf{p}_0)$, where K is the update factor (a positive integer chosen by the user), consists approximately² of all lattice points $\mathbf{p} \in \mathcal{I}$ such that $\mathbf{p} \neq \mathbf{p}_0$ and the l_2 distance $\|\mathbf{p} - \mathbf{p}_0\|_2 \leq K$. It is used for updating **Considered** points. Correspondingly, the far neighborhood of the mesh point \mathbf{x}_0 is defined as

$$\mathcal{N}_{\text{far}}^K(\mathbf{x}_0) := \{\mathbf{x} \mid \mathbf{p} \in \mathcal{N}_{\text{far}}^K(\mathbf{p}_0)\}.$$

²More precisely, $\mathbf{p} \in \mathcal{N}_{\text{far}}^K(\mathbf{p}_0)$ iff $\mathbf{p} \neq \mathbf{p}_0$, $\mathbf{p} \in \mathcal{I}$, and $|i - i_0| \leq K$, $|j - j_0| \leq \text{ceil}(\sqrt{K^2 - |i - i_0|^2})$, and $|k - k_0| \leq \text{ceil}(\sqrt{K^2 - \min\{|i - i_0|^2 + |j - j_0|^2, K^2\}})$. Defined so, $\mathbf{p} \in \mathcal{N}_{\text{far}}^K(\mathbf{p}_0)$ is slightly larger than $\{\mathbf{p} \in \mathcal{I} \mid \mathbf{p} \neq \mathbf{p}_0, \|\mathbf{p} - \mathbf{p}_0\|_2 \leq K\}$.

If the mesh steps in x_i , $i = 1, 2, 3$, are all equal to h then the far neighborhood of \mathbf{x}_0 is approximately the ball centered at \mathbf{x}_0 of radius Kh .

At the start, all mesh points are **Unknown**. Initialization consists in computing tentative values at the mesh points lying near the attractor, switching their status to **Considered**, and adding them to the binary tree. The binary tree maintains the heap sort of the values at **Considered** points so that the smallest **Considered** value is always at the root of the tree. At each step of the main body of the OLIM, a **Considered** mesh point \mathbf{x}_{new} with the smallest tentative value becomes **Accepted Front**. Then the hierarchical update procedure proposed in [11] and further developed in [38] is implemented. It consists of two substeps. First, for all **Considered** points in $\mathcal{N}_{\text{far}}^K(\mathbf{x}_{\text{new}})$ proposed update values involving \mathbf{x}_{new} are computed. Second, each **Unknown** point \mathbf{x} in $\mathcal{N}_{\text{near}}(\mathbf{x}_{\text{new}})$ becomes **Considered** and a tentative value at \mathbf{x} is computed using the **Accepted Front** points in $\mathcal{N}_{\text{far}}^K(\mathbf{x})$. This algorithm is summarized in the pseudocode below. The details of each step are elaborated in [38].

Initialization *Start with all mesh points being Unknown. Set values of U at them to ∞ . Let \mathbf{x}^* be an asymptotically stable equilibrium located at a mesh point. Compute tentative values of U at the points $\mathbf{x} \in \mathcal{N}_{\text{near}}(\mathbf{x}^*)$ and change their status to Considered.*

The main body

while *the boundary of the mesh has not been reached and the set of Considered points is not empty* **do**

1: Change the status of the **Considered** point \mathbf{x}_{new} with the smallest tentative value of U to **Accepted Front**.

2: Change the status of all **Accepted Front** points in $\mathcal{N}_{\text{near}}(\mathbf{x}_{\text{new}})$ that no longer have **Considered** points in their $\mathcal{N}_{\text{near}}$ -neighborhoods to **Accepted**.

3: Update all **Considered** points $\mathbf{x} \in \mathcal{N}_{\text{far}}^K(\mathbf{x}_{\text{new}})$. The updates must involve \mathbf{x}_{new} .

4: Change the status of each **Unknown** point $\mathbf{x} \in \mathcal{N}_{\text{near}}(\mathbf{x}_{\text{new}})$ to **Considered** and update them using the **Accepted Front** points in $\mathcal{N}_{\text{far}}^K(\mathbf{x})$.

end

Algorithm 1: A coarse-grained pseudocode of the OLIM.

Now we outline the hierarchical update strategy. All details of it are worked out in [38]. There are three types of updates done in the following order:

one-point updates \rightarrow triangle updates \rightarrow simplex updates.

Let \mathbf{x} be a **Considered** point to be updated, and $\mathbf{y} \in \mathcal{N}_{\text{far}}^K(\mathbf{x})$ be **Accepted Front**.

One-point update. We connect \mathbf{x} and \mathbf{y} with a line segment and approximate the geometric action (9) along it using the midpoint quadrature rule $\mathcal{Q}_M(\mathbf{y}, \mathbf{x})$. Then the proposed value of the quasipotential at \mathbf{x} is

$$Q_1(\mathbf{y}, \mathbf{x}) = U(\mathbf{y}) + \mathcal{Q}_M(\mathbf{y}, \mathbf{x}). \quad (17)$$

If $Q_1(\mathbf{y}, \mathbf{x})$ is less than the current tentative value $U(\mathbf{x})$, we replace $U(\mathbf{x})$ with it. Otherwise, we leave $U(\mathbf{x})$ unchanged. Furthermore, we compare $Q_1(\mathbf{y}, \mathbf{x})$ with the current minimizer of the one-point update at \mathbf{x} and update it if $Q_1(\mathbf{y}, \mathbf{x})$ is smaller. In step 3 of Algorithm 1, the only one-point update computed is $Q_1(\mathbf{x}_{\text{new}}, \mathbf{x})$. In step 4, one-point updates are computed for all **Accepted Front** points $\mathbf{y} \in \mathcal{N}_{\text{far}}^K(\mathbf{x})$.

Triangle update. Triangle updates always involve the minimizer of the one-point update \mathbf{x}_0 . The base of an admissible triangle is a line segment connecting \mathbf{x}_0 and an **Accepted Front** point \mathbf{x}_1 satisfying $\|\mathbf{p}_1 - \mathbf{p}_0\|_1 \leq 2$ and $\|\mathbf{p}_1 - \mathbf{p}_0\|_\infty = 1$ where \mathbf{p}_0 and \mathbf{p}_1 are the indices of

\mathbf{x}_0 and \mathbf{x}_1 respectively. The points on the line segment $[\mathbf{x}_0, \mathbf{x}_1]$ are parametrized by $\lambda \in [0, 1]$: $\mathbf{x}_\lambda := \mathbf{x}_0 + \lambda(\mathbf{x}_1 - \mathbf{x}_0)$. The values of U on $[\mathbf{x}_0, \mathbf{x}_1]$ are found by linear interpolation: $U(\mathbf{x}_\lambda) \equiv U_\lambda := U(\mathbf{x}_0) + \lambda(U(\mathbf{x}_1) - U(\mathbf{x}_0))$. Then the triangle update is done by solving the constrained minimization problem

$$Q_2(\mathbf{x}_0, \mathbf{x}_1, \mathbf{x}) = \min_{\lambda \in [0,1]} \{U_\lambda + \mathcal{Q}_M(\mathbf{x}_\lambda, \mathbf{x})\} \quad (18)$$

and replacing the current tentative value $U(\mathbf{x})$ with the proposed value $Q_2(\mathbf{x}_0, \mathbf{x}_1, \mathbf{x})$ if and only if the latter is less than the former. This replacement may take place only if an interior point solution is found. Hence, we are interested in the solution to (18) only if the minimizer $\lambda^* \in (0, 1)$. Therefore, we take the derivative of the function being minimized in the right-hand side of (18), compare its signs at the endpoints, and proceed with solving the nonlinear equation only if the signs are different.

Simplex update. One of the vertices of the triangle at the base of an admissible simplex must be the minimizer of the one-point update \mathbf{x}_0 , and one of its sides adjacent to \mathbf{x}_0 , let's call it $[\mathbf{x}_0, \mathbf{x}_1]$, must be such that the constrained minimization problem (18) has given an inner point solution $\lambda^* \in (0, 1)$. The third vertex of the base of an admissible simplex must be an **Accepted Front** point \mathbf{x}_2 such that l_∞ distances between the indices of \mathbf{x}_0 , \mathbf{x}_1 , and \mathbf{x}_2 are all 1, and at most one of the l_1 distances between their indices is 2, while the other ones are 1. The proposed value produced by the simplex update is the solution of the constrained minimization problem

$$Q_3(\mathbf{x}_0, \mathbf{x}_1, \mathbf{x}_2, \mathbf{x}) = \min_{\lambda \in [0,1]} \{U_\lambda + \mathcal{Q}_M(\mathbf{x}_\lambda, \mathbf{x})\}, \quad (19)$$

$$\text{where } \mathbf{x}_\lambda = \mathbf{x}_0 + \lambda_1(\mathbf{x}_1 - \mathbf{x}_0) + \lambda_2(\mathbf{x}_2 - \mathbf{x}_0),$$

$$U_\lambda = U(\mathbf{x}_0) + \lambda_1(U(\mathbf{x}_1) - U(\mathbf{x}_0)) + \lambda_2(U(\mathbf{x}_2) - U(\mathbf{x}_0)),$$

$$\text{subject to } \lambda_1 \geq 0, \quad \lambda_2 \geq 0, \quad \lambda_1 + \lambda_2 \leq 1. \quad (20)$$

The warm start for solving (19) is the vector $\lambda := [\lambda^*, 0]$ where λ^* is the minimizer of (18). As we do it for the triangle update, we wish to quickly reject the simplex update if its minimizer is certainly lying on the boundary of the triangle (20). We use the Karush-Kuhn-Tucker (KKT) optimality conditions (see [25], Chapter 12) to do so. They boil down (see Appendix C) to checking whether

$$\frac{\partial}{\partial \lambda_2} (U_\lambda + \mathcal{Q}_M(\mathbf{x}_\lambda, \mathbf{x})) \geq 0. \quad (21)$$

If (21) holds, then $[\lambda^*, 0]$ is a local solution to (19), and hence we reject the simplex update. Otherwise we proceed with numerical minimization using Newton's method. If an interior point solution is found, we replace the current tentative value $U(\mathbf{x})$ with $Q_3(\mathbf{x}_0, \mathbf{x}_1, \mathbf{x}_2, \mathbf{x})$ provided that $Q_3(\mathbf{x}_0, \mathbf{x}_1, \mathbf{x}_2, \mathbf{x}) < U(\mathbf{x})$. Otherwise, $U(\mathbf{x})$ remains unchanged.

We remark that the computation of the quasipotential terminates as soon as a boundary mesh point becomes **Accepted Front**. This is important because the MAP that leaves the computational domain via this point might return to it, and it is crucial for an accurate computation of the quasipotential that the computation follows the MAPs.

4.2 Challenges of computing the quasipotential for stochastic Lorenz'63

An important characteristic of the vector field in SDE (1) in a neighborhood of an attractor A is the ratio of the magnitude of the rotational component to that of the potential one [38]:

$$\Xi(\mathbf{x}) := \frac{\|\mathbf{l}(\mathbf{x})\|}{\|^{1/2}\nabla U(\mathbf{x})\|}. \quad (22)$$

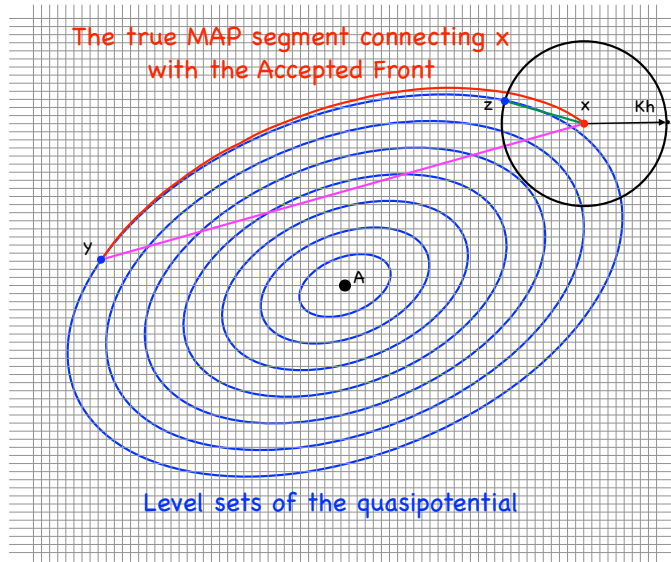


Figure 1: An illustration for the difficulty of computing the quasipotential in the case where the ratio $\Xi(\mathbf{x})$ given by (22) is large. The blue closed curves represent some level sets of the quasipotential. \mathbf{x} is a Considered point that is up for an update. The green segment $[\mathbf{z}, \mathbf{x}]$ is the best linear approximation to the MAP connecting \mathbf{x} with the Accepted Front within the given update radius Kh .

If $\Xi(\mathbf{x})$ is not too large (does not exceed 10) in the basin of A , except, perhaps some small neighborhoods of the attractor or the escape state, the OLIMs give accurate results on uniform rectangular meshes of reasonable sizes [11, 12, 38]. However, if $\Xi(\mathbf{x})$ is large (much larger than 10) in a significant part of the basin of A , the accuracy of the numerical solution by the OLIM on a regular rectangular mesh deteriorates (see Section 4 in [11]). The problem is illustrated in Fig. 1. Suppose the computation has reached the level set of the quasipotential depicted with the largest closed blue curve. All mesh points inside it are either Accepted if they have no Unknown or Considered nearest neighbors, or Accepted Front, if they do. Let \mathbf{x} be a Considered point up for an update. If $\Xi(\mathbf{x})$ is large, the segment of the MAP arriving at \mathbf{x} from the span of Accepted Front mesh points is long. A rough estimate for its length is $\Xi(\mathbf{x})h$ where h is the mesh step. Let \mathbf{y} be the point where this MAP segment starts at the span of the Accepted Front. Even if the update factor K were chosen large enough so that \mathbf{y} lies in the ball centered at \mathbf{x} of radius Kh , the straight line segment (the magenta line segment from \mathbf{x} to \mathbf{y} in Fig. 1) and the midpoint quadrature rule would give poor approximations for the MAP segment and the geometric action along it respectively resulting in an inaccurate update value at \mathbf{x} . It is shown in [11, 38] that too large update factor may deteriorate the accuracy. A safer but still too rough approximate solution would be obtained if the update radius is reasonably small, i.e., chosen according to the proposed rules of thumb in [11, 38]. Then the segment of MAP would be approximated with the green line segment $[\mathbf{z}, \mathbf{x}]$ in Fig. 1.

Now imagine the case where $\Xi(\mathbf{x}) \sim 10^3$ as it is for stochastic Lorenz'63 with $\rho_1 < \rho < \rho_2$ where the stable equilibria and the strange attractor coexist. 3D computations on regular rectangular meshes will give a qualitative idea about the geometry of the level sets of the quasipotential, but the found quasipotential barriers will be completely off.

The ratio $\Xi(\mathbf{x})$ for the Lorenz system at $1 < \rho < \rho_2 \approx 24.74$ can be estimated from that for the linearized system at C_+ (see Appendix D). The graph of Ξ for the linearized system is displayed in Fig. 2. It shows that the maximum of $\Xi(\mathbf{x})$ blows up as $\rho \rightarrow \rho_2$. At $\rho = 24.4$, the largest ρ at which we present the results of our computations, the maximal value of $\Xi(\mathbf{x})$ for the linearized system is 973.4.

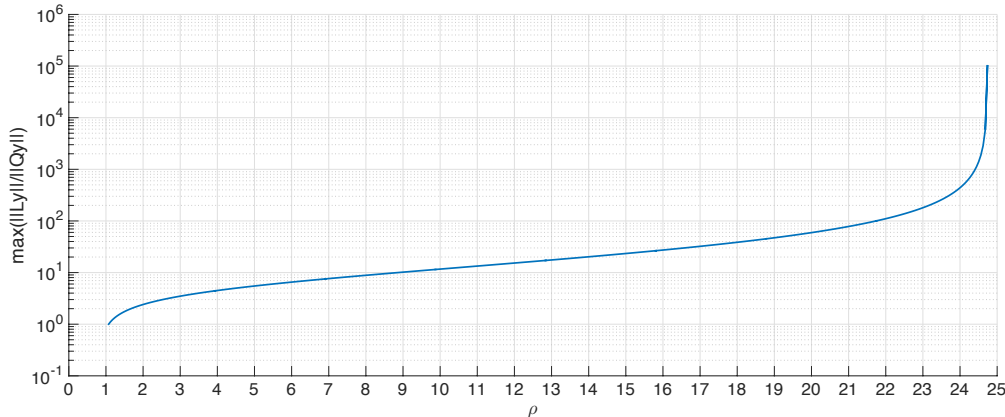


Figure 2: The graph of the maximal ratio Ξ of the magnitudes of the rotational and potential components of the linear SDE $dy = Jydt + \sqrt{\epsilon}dw$ where J is the Jacobian matrix of the right-hand side of the Lorenz system (16) evaluated at the equilibrium C_+ for the range $1 < \rho < \rho_2 \approx 24.74$ where C_+ is asymptotically stable.

Challenged by this problem, we have developed an approach that allows us to obtain reasonably accurate values of the quasipotential barriers. It consists in finding approximate 2D manifolds (or unions of 2D manifolds) where the MAPs emanating from the attractor are located, building so-called radial meshes on them, and adjusting the OLIM for performing computations on radial meshes. This approach is suitable for any 3D SDE where the level sets of the quasipotential are thin, i.e., close to some 2D manifolds (see Assumption 1 below), which can be determined by visual inspection of the computed 3D level sets. Note that this is a safe diagnosis as the 3D OLIM tends to make the level sets thicker than the true ones if $\Xi(\mathbf{x})$ is large. In this case, the MAP going from the attractor to the escape state will be very close to any 2D manifold (or union of manifolds) approximating the level set containing the escape state. We find such a manifold using the characteristics of the corresponding ODE. The following lemma is instrumental for this approximation.

Lemma 4.1. *Let A be an attractor of $\dot{\mathbf{x}} = \mathbf{b}(\mathbf{x})$, where $\mathbf{b} \in C^1(\mathbb{R}^3)$. Let*

$$\mathcal{V}_a := \{\mathbf{x} \in \mathbb{R}^3 \mid U(\mathbf{x}) \leq a\}$$

be a sublevel set of the quasipotential completely lying in the basin of A , and γ be a curve lying on the boundary of \mathcal{V}_a , i.e., for any $\mathbf{x} \in \gamma$, $U(\mathbf{x}) = a$. Let \mathcal{M}' and \mathcal{M} be the manifolds consisting, respectively, of the MAPs going from A to γ , and the characteristics starting at γ and running to A . Then $\mathcal{M}' \subset \mathcal{V}_a$ and $\mathcal{M} \subset \mathcal{V}_a$.

A proof of Lemma 4.1 is found in Appendix E.

Let γ be an unstable limit cycle serving as the escape state from the basin of an attractor A . Let the quasipotential at γ be U_γ . We can consider a sublevel set \mathcal{V}_a for $a < U_\gamma$ and arbitrarily

close to U_γ . By Lipschitz continuity of the quasipotential [4], a can be chosen so that the distance between γ and \mathcal{V}_a is smaller than any given positive number. Correspondingly, we can pick a curve γ' lying on the boundary of \mathcal{V}_a located arbitrarily close to the limit cycle γ . By Lemma 4.1, the manifolds \mathcal{M}' and \mathcal{M} consisting of MAPs/characteristics running to/from γ' will lie in \mathcal{V}_a .

Assumption 1. *Suppose that the level set \mathcal{V}_a is close to both manifolds \mathcal{M} and \mathcal{M}' , i.e., the Housdorff distances³ between \mathcal{V}_a and \mathcal{M} and between \mathcal{V}_a and \mathcal{M}' are less than some small $\delta > 0$:*

$$d_H(\mathcal{V}_a, \mathcal{M}) < \delta \quad \text{and} \quad d_H(\mathcal{V}_a, \mathcal{M}') < \delta.$$

Under Assumption 1, the triangle inequality implies that the Housdorff distance between \mathcal{M} and \mathcal{M}' is bounded by 2δ :

$$d_H(\mathcal{M}, \mathcal{M}') \leq d_H(\mathcal{M}, \mathcal{V}_a) + d_H(\mathcal{M}', \mathcal{V}_a) < 2\delta. \quad (23)$$

We will employ Assumption 1 for $15 \leq \rho \leq 24.4$. Figs. 7 and 9 below illustrate it: compare the MAPs (the dark red curves) and the characteristics (the dark blue curves) in these figures and observe that they lie on close manifolds located inside visibly thin level sets.

Note that the manifold \mathcal{M} can be readily sampled by shooting characteristics from γ' to A . In the next section, we describe how to build radial meshes on \mathcal{M} , adjust the OLIM for them, and test its performance.

4.3 Radial meshes on manifolds

We call a mesh *radial* if it is set up as follows. Let γ_0 be a point or a closed curve, and let γ be another closed curve. We pick a finite set of simple closed curves that do not intersect pairwise and index them γ_i , $i = 1, \dots, N_r - 2$. We add γ_0 and $\gamma_{N_r-1} \equiv \gamma$ to this set. These curves will be referred to as *parallels*. We also pick a finite set of curves, *meridians*, going from γ_0 to γ and crossing each γ_i exactly once in the order of increase of their indices. We index the meridians from 0 to $N_a - 1$ and identify meridian 0 with meridian N_a . The resulting mesh has size $N_r \times N_a$. Examples of radial meshes for the Lorenz system defined on manifolds consisting of all characteristics going from saddle cycles to asymptotically stable equilibria at $\rho = 15$ and $\rho = 24.4$ are shown in Figs. 8(a) and 13(a) respectively. A radial mesh defined between two closed curves, the saddle cycle γ_- and a closed curve approximating an “eye” of the strange attractor at $\rho = 24.4$, is displayed in Fig. 14(a). Our technique for building radial meshes is described in Appendix F and implemented in the Matlab code `make2Dmesh.m`.

To adjust the OLIM for radial meshes, we redefine the neighborhood $\mathcal{N}_{far}((i_r, i_a))$ from which a mesh point indexed (i_r, i_a) can be updated using two update factors, radial K_r and angular K_a , as follows: $\mathcal{N}_{far}((i_r, i_a))$ consists of all mesh points (j_r, j_a) satisfying

$$\max\{0, i_r - K_r\} \leq j_r \leq \min\{i_r + K_r, N_r - 1\} \quad \text{and} \\ |(j_a - i_a) \bmod N_a| \leq K_a.$$

Let us check whether the OLIM applied to a system with large ratio Ξ produces small enough errors on 2D radial meshes of reasonable sizes and these errors properly decay with mesh refinement.

³ $d_H(\mathcal{X}, \mathcal{Y}) = \max\{\sup_{\mathbf{x} \in \mathcal{X}} \inf_{\mathbf{y} \in \mathcal{Y}} \|\mathbf{x} - \mathbf{y}\|, \sup_{\mathbf{y} \in \mathcal{Y}} \inf_{\mathbf{x} \in \mathcal{X}} \|\mathbf{x} - \mathbf{y}\|\}.$

We set up an ad hoc 2D example with an asymptotically stable spiral point at the origin and an unstable limit cycle $\|\mathbf{x}\| = 1$:

$$\begin{bmatrix} dx_1 \\ dx_2 \end{bmatrix} = \begin{bmatrix} \|\mathbf{x}\|^2 - 1 & a \\ -a & \|\mathbf{x}\|^2 - 1 \end{bmatrix} \begin{bmatrix} x_1 \\ x_2 \end{bmatrix} dt + \sqrt{\epsilon} d\mathbf{w}. \quad (24)$$

We pick $a = 10^3$, then $\Xi \geq 10^3$. The exact quasipotential for (24) with respect to the origin is given by

$$U(\mathbf{x}) = \begin{cases} \|\mathbf{x}\|^2 (1 - 0.5\|\mathbf{x}\|^2) & \|\mathbf{x}\| \leq 1 \\ 0.5, & \|\mathbf{x}\| > 1 \end{cases}. \quad (25)$$

We have conducted two experiments with computing the quasipotential for (24). The goal of the first experiment is to establish the dependence of the numerical error on the relationship between N_r , N_a , K_r , and K_a . We set $N_r = 1024$ and run the solver for $N_a = 2^q N_r$, $q = 0, 1, 2, 3$, and K_r varying from 1 to $\text{round}(N_r/40) = 25$ and $K_a = 2^q K_r$, respectively. The computational domain is the unit circle. The dependence of the normalized maximal absolute error

$$E := \frac{\max_{i_r, i_a} |U(i_r, i_a) - U_{\text{exact}}(i_r, i_a)|}{\max_{i_r, i_a} U_{\text{exact}}(i_r, i_a)} \quad (26)$$

on K_r is shown in Fig. 3(a). The normalized maximal absolute error (the red curve) for the 1024×1024 rectangular mesh defined on the square $[-1, 1]^2$ is also provided for comparison. These results eloquently demonstrate the superiority of the radial meshes for computing the quasipotential in the case where the ratio Ξ is large. Also, the choice $K_r = \text{round}(N_r/40)$ and $K_a = \text{round}(N_a/40)$ is reasonable and can be used as a default setting for radial meshes.

The goal of the second experiment is to verify error decay with mesh refinement. We have run computations with $N_r = 2^p$, $p = 8, 9, 10, 11, 12$, $N_a = 2N_r$, $K_r = \text{round}(N_r/40)$, and $K_a = 2K_r$. The plot of the normalized maximal absolute error in Fig. 3(b) shows the desired convergence. The least squares fit gives a superquadratic convergence:

$$E = 3.3 \cdot 10^4 \cdot N_r^{-2.2}. \quad (27)$$

The superiority of radial meshes over rectangular ones for the computation of the quasipotential in the basins of spiral point attractors of vector fields with large rotational components is due to the fact that the radial meshes have update regions better adjusted to the geometry of the MAPs than the rectangular ones. This phenomenon is illustrated in Fig. 4. The update regions of radial meshes are small near the equilibrium where the MAP has high curvature and grow away from it where the MAP's curvature decreases. In contrast, the update regions of rectangular meshes remain uniform. As a result, they are too large near the equilibrium and not large enough away from it.

In summary, our experiments with SDE (24) with a stable spiral point, an unstable limit cycle, and $\Xi \geq 10^3$ have demonstrated that the computation of the quasipotential on radial meshes of moderate sizes gives accurate and reliable results.

Remark 4.1. *We emphasize that we still use line segments in the OLIM on radial meshes to approximate MAP segments. We have explored a variant of OLIM where the minimizer for each local constraint minimization problem is sought on the set of curves of the following form:*

$$\{(r(t), \theta(t)) \mid t \in [0, 1], r(t) = r_1 + t(r_2 - r_1), \theta(t) = \theta_1 + t(\theta_2 - \theta_1)\}$$

where (r_i, θ_i) , $i = 1, 2$, are the polar coordinates of the endpoints of the curve. We have found that the use of line segments as in the original OLIM gives more accurate results, so we stick with line segments.

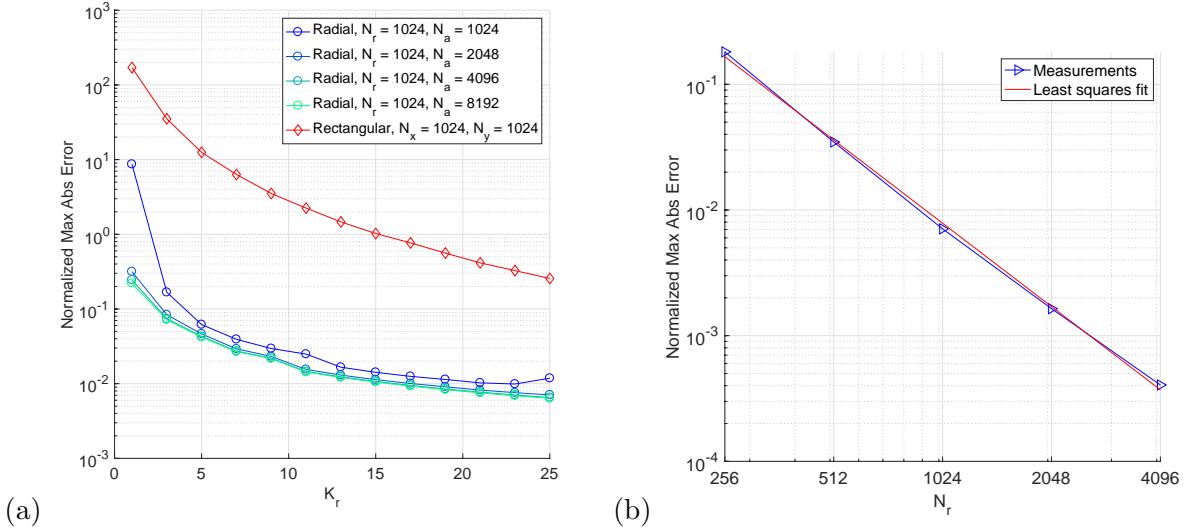


Figure 3: Measurements of numerical errors for radial meshes $N_r \times N_a$ in computing the quasipotential for SDE (24). (a): The dependence of the normalized maximal absolute error (26) on the update parameter K_r . The parameter K_a was chosen so that $N_a/N_r = K_a/K_r$. (b): The dependence of the normalized maximal absolute error (26) (the blue plot) on N_r with $N_a = 2N_r$, $K_r = \text{round}(N_r/40)$, and $K_a = 2K_r$. The least squares fit (27) is included for comparison.

5 Results

In this section, we present a collection of plots of the level sets of the computed quasipotential in 3D for the Lorenz system at $\rho = 0.5, 12, 15, 20$, and 24.4 . Where appropriate, we perform 2D computations on radial meshes on manifolds and refine the estimates for the quasipotential barriers between different basins or regions of the phase space. Our collection of MAPs computed by integrating (13) backwards in s (code `ShootMAPs.c`, [5]) can be compared with that obtained in [40] for somewhat different set of values of ρ using the minimum action method (MAM). Note that, while the MAM is easier to program than the OLIM and it is suitable for any phase-space dimension, its output is biased by the initial guess for the path and hence might converge to a local minimizer in the path-space instead of the global one. Furthermore, MAM does not allow one to visualize the level sets of the quasipotential. Estimates for quasipotential barriers are not provided in [40] while we do it here.

5.1 $0 < \rho < 1$

For $0 < \rho < 1$, the origin is globally attracting. Two level sets of the quasipotential for $\rho = 0.5$ are shown in Fig. 5. The computation was performed on $513 \times 513 \times 513$ mesh with the update factor $K = 14$. This choice of K for $N = 513$ was suggested in [38]. The level sets are heart-shaped and oriented approximately along the plane $x_1 = x_2$. Let X be a level set and let γ_X be the intersection of X with the vertical plane $x_1 = x_2$. The curve γ_X runs approximately along the edge of the heart-shaped level set X . We pick X to be a level set corresponding to one of the largest computed values of the quasipotential and find a collection of points marked with large orange dots lying on the corresponding curve γ_X and forming angles from 0 to 2π with step $\pi/72$. The characteristics of

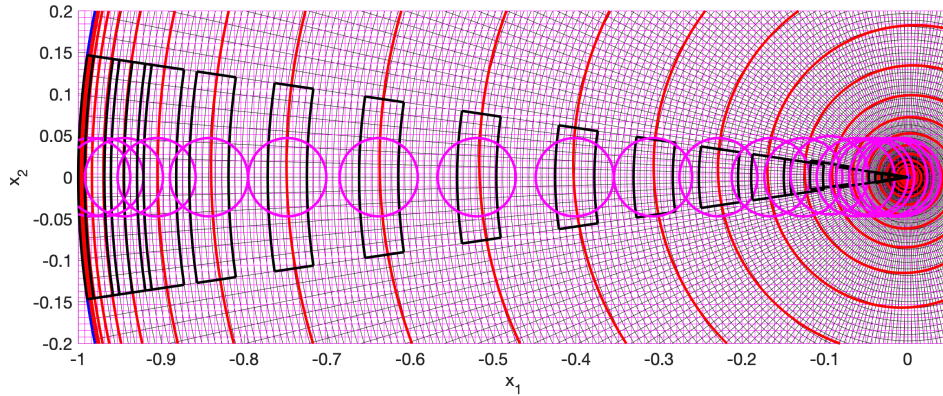


Figure 4: An illustration explaining the advantage of radial meshes over rectangular ones for the computation of the quasipotential on the example of SDE (24) with $a = 40$. Two computations were performed. The first one was done on the radial mesh with $N_r = 128$, $N_a = 256$, $K_r = 3$, $K_a = 6$. The maximal absolute and RMS errors for this computations are $1.00 \cdot 10^{-2}$ and $2.44 \cdot 10^{-3}$ respectively. The second computation was performed on the rectangular mesh with $N = 256$ and $K = 6$ and gave the maximal absolute and RMS errors of $1.39 \cdot 10^{-1}$ and $6.43 \cdot 10^{-2}$ respectively which are more than an order of magnitude larger than those for the radial mesh. The CPU times for the radial and rectangular meshes are approximately the same: 0.24 and 0.22 seconds respectively, The thick red curve is the exact MAP going from the equilibrium at the origin to the unstable limit cycle $r = 1$. The thin black mesh is the radial mesh. The thick black curves bound some samples of its update regions. The thin magenta mesh is the rectangular mesh, and the thick magenta circles are samples of its update regions.

(16) (the dark blue curves) and the MAPs of (2) (the dark red curves) starting and arriving at this set of points, respectively, are notably different. The set of characteristics starting at γ_X and the set of MAPs arriving at γ_X form visibly distinct 2D manifolds.

Let us find the directions along which typical characteristics and typical MAPs approach the origin and emanate from it, respectively. It is hard to see in Fig. 5 whether they coincide or not. Let J be the Jacobian matrix of the right-hand side of (16) evaluated at the origin:

$$J = \begin{bmatrix} -\sigma & \sigma & 0 \\ \rho & -1 & 0 \\ 0 & 0 & -\beta \end{bmatrix}. \quad (28)$$

For the linear SDE

$$d\mathbf{x} = J\mathbf{x}dt + \sqrt{\epsilon}d\mathbf{w}, \quad (29)$$

the quasipotential decomposition is given by $J\mathbf{x} = -Q\mathbf{x} + L\mathbf{x}$ (see Appendix D), where Q and L are matrices. The quasipotential is the quadratic form $U(\mathbf{x}) = \mathbf{x}^\top Q\mathbf{x}$ where Q can be found analytically [4]:

$$Q = \begin{bmatrix} Q_1 & \\ & \beta \end{bmatrix}, \quad \text{where} \quad (30)$$

$$Q_1 = \frac{\sigma + 1}{d} \begin{bmatrix} \sigma(\sigma + 1) + \rho(\rho - \sigma) & -\rho - \sigma^2 \\ -\rho - \sigma^2 & (\sigma + 1) - \sigma(\rho - \sigma) \end{bmatrix}, \quad (31)$$

$$d = (\sigma + 1)^2 + (\rho + \sigma)^2.$$

The rotational matrix $L = J + Q$ is

$$L = \begin{bmatrix} L_1 & \\ & 0 \end{bmatrix}, \quad \text{where} \quad (32)$$

$$L_1 = \frac{\rho - \sigma}{d} \begin{bmatrix} \rho + \sigma^2 & -(\sigma + 1) + \sigma(\rho - \sigma) \\ \sigma(\sigma + 1) + \rho(\rho - \sigma) & -\rho - \sigma^2 \end{bmatrix}.$$

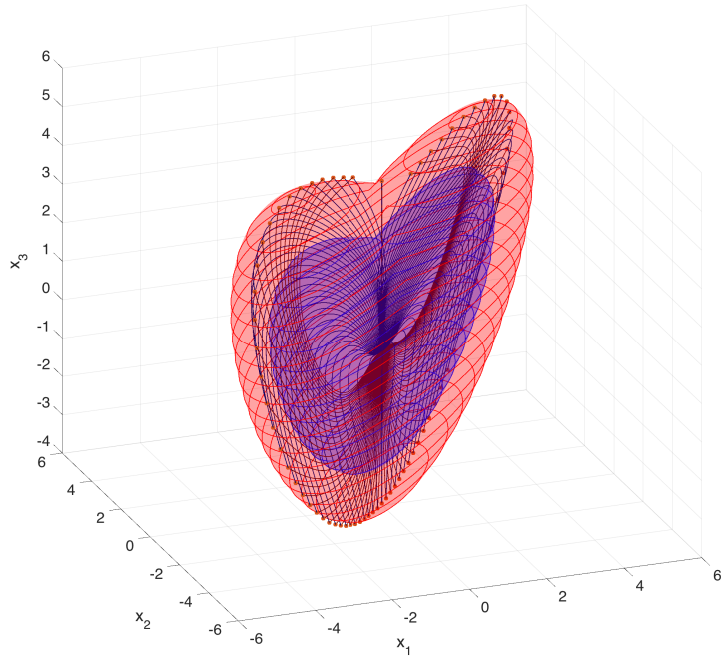
For the linear SDE (29), MAPs are the characteristics of $\dot{\mathbf{x}} = (Q + L)\mathbf{x}$. Obtaining spectral decompositions of $J = -Q + L$ and $\tilde{J} = Q + L$ for $\rho = 0.5$ we find that typical characteristics of (16) approach the origin tangent to the line $\text{span}(\mathbf{v})$, while typical MAPs emanate from the origin tangent to the line $\text{span}(\tilde{\mathbf{v}})$, where

$$\mathbf{v} \approx \begin{bmatrix} 0.7241 \\ 0.6897 \\ 0 \end{bmatrix}, \quad \tilde{\mathbf{v}} \approx \begin{bmatrix} 0.6924 \\ 0.7215 \\ 0 \end{bmatrix}. \quad (33)$$

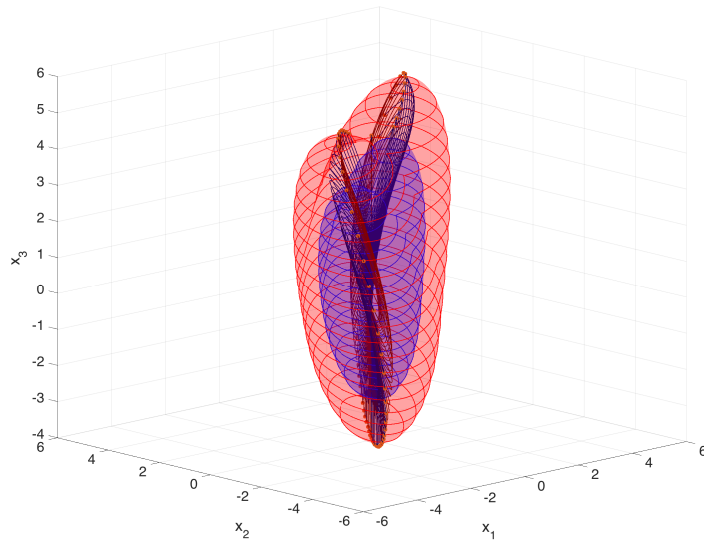
5.2 $1 < \rho < \rho_0 \approx 13.926$

In this interval, the equilibria C_\pm switch from stable nodes to stable spiral points at $\rho \approx 2.1546$. Fig. 6 displays the level sets of the quasi-potential for $\rho = 12$ with respect to each stable equilibrium. It was computed on a $513 \times 513 \times 513$ mesh with $K = 14$. The found value of the quasipotential at the origin that serves as the transition state between C_\pm is 19.47. Therefore, at $\rho = 12$, the expected escape time from the basin of C_+ scales as

$$\mathbb{E}[\tau_{C_+}] \asymp e^{19.47/\epsilon}. \quad (34)$$



(a)



(b)

Figure 5: Two views of the level sets of the quasipotential at $\rho = 0.5$ corresponding to $U = 20$ (the blue surface) and $U = 40$ (the red surface). The thin blue and red closed curves lying on the corresponding level sets are shown to aid 3D visualization. The dark blue curves depict a collection of the characteristics starting at the set of points marked by large orange dots and approaching the origin. The dark red curves represent a collection of the MAPs emanating from the origin and arriving at the same set of points. A movie with this figure rotating around the x_3 -axis is available at <https://youtu.be/YscXN18lgyU>.

The MAP from C_+ to C_- is obtained by the concatenation of the computed MAP from C_+ to the origin (the dark red curve starting at C_+) and the characteristic from the origin to C_- (the dark blue curve ending at C_-). Fig. 6(b) shows that the MAPs and the characteristics connecting C_{\pm} and the origin lie on close 2D manifolds.

We did a consistency check by finding the quasipotential barrier by integrating the geometric action (9)-(10) along the found MAP and got the value 19.89 that is at a reasonable agreement with 19.47 found by our 3D computation.

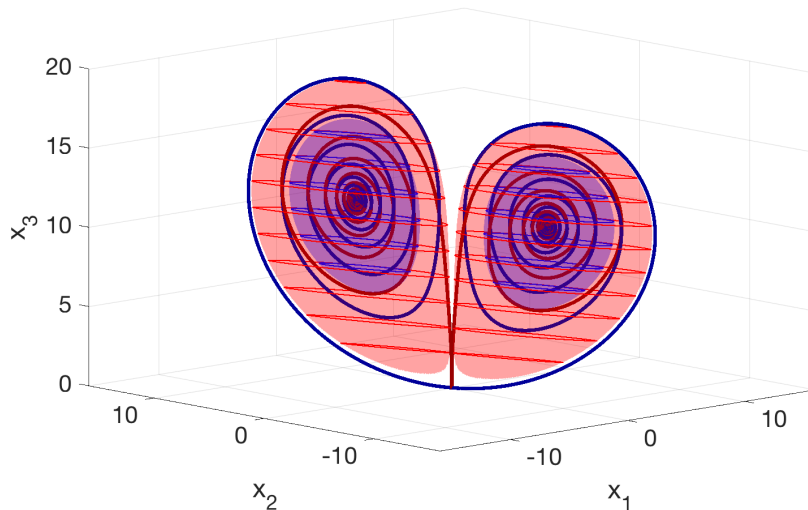


Figure 6: The level sets of the quasipotential at $\rho = 12$ corresponding to $U = 10$ (the blue surface) and $U = 19.42$ (the red surface). The dark blue curves are the characteristics emanating from the origin along its unstable directions $\pm\xi$ (42) and arriving at C_{\pm} respectively. The dark red curves are the MAPs going from C_{\pm} to the origin. The MAP from C_{\pm} to C_{\mp} is obtained by the concatenation of the MAP from C_{\pm} to the origin (a dark red curve) and the characteristic from the origin to C_{\mp} (a dark blue curve). A movie with this figure rotating around the x_3 -axis is available at <https://youtu.be/-ABbuD8oDjI>.

5.3 $13.926 \approx \rho_0 < \rho < \rho_1 \approx 24.06$

In this range, the escape states from C_+ and C_- are the saddle limit cycles γ_+ and γ_- respectively. We have computed the quasipotential for two values of ρ : $\rho = 15$ and $\rho = 20$.

5.3.1 $\rho = 15$

The computed quasipotential for $\rho = 15$ with respect to C_+ is visualized in Fig. 7. First, we picked a large computational domain to embrace the level set of the quasipotential enclosing both

of the stable equilibria C_{\pm} and used a $613 \times 613 \times 613$ mesh and $K = 15$. Second, we chose a smaller domain just to enclose γ_+ . It was a cube with side 13 centered at C_+ , and the mesh in it was $1001 \times 1001 \times 1001$. K was set to 20. The found quasipotential is nearly constant on γ_+ : it varies between 17.42 and 17.45. The saddle cycles γ_{\pm} are depicted with thick bright red curves. A maximum likelihood transition path from C_+ to C_- can be obtained by the concatenation of a MAP from C_+ to γ_+ , the saddle cycle γ_+ , and a characteristic going from γ_+ to C_- . One such MAP and one such characteristic are the dark red and dark blue curves in Fig. 7 respectively.

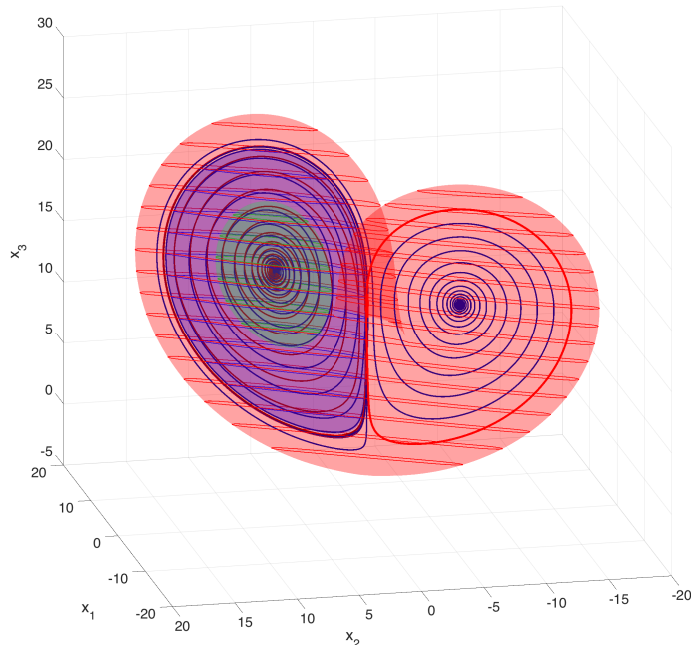
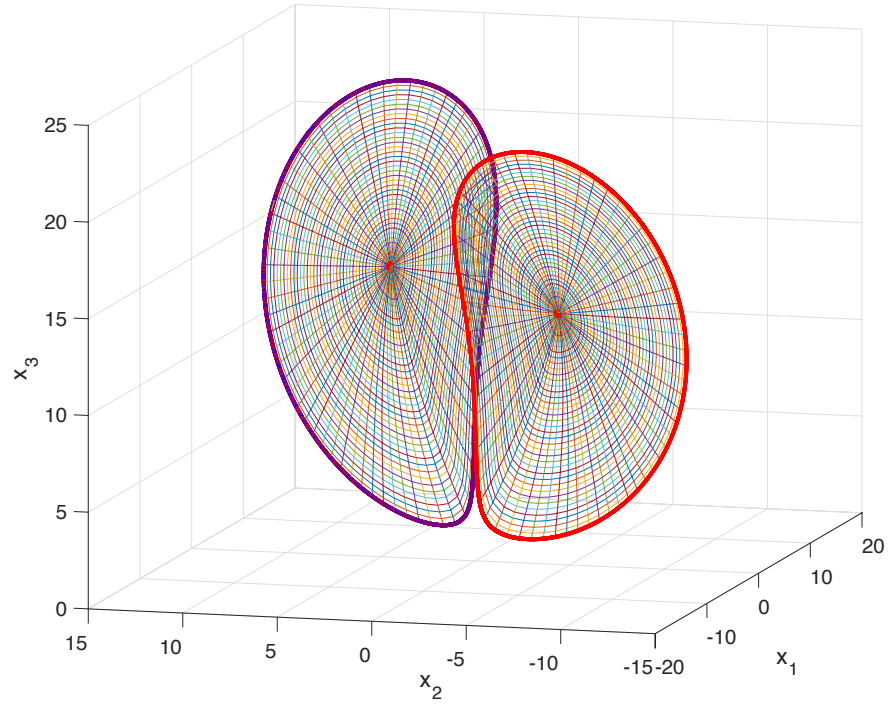
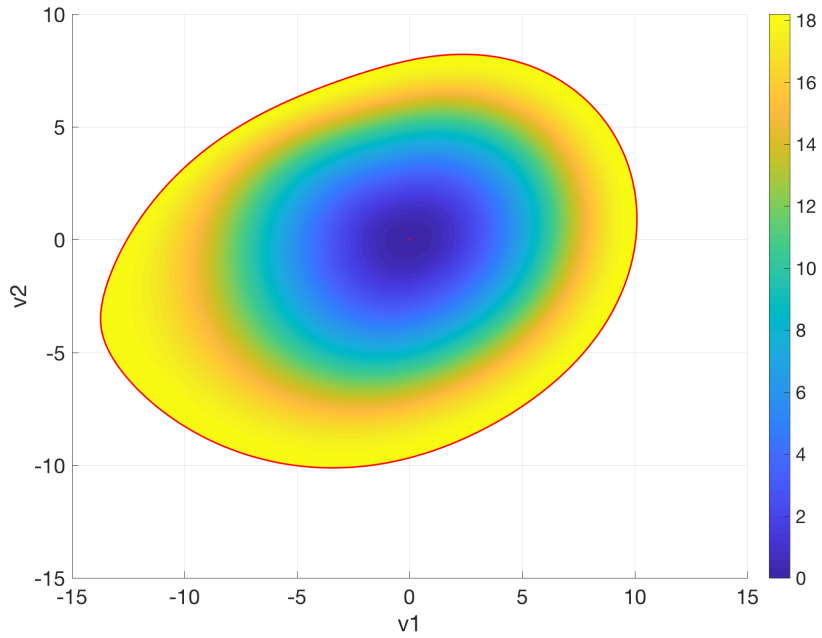


Figure 7: The level sets of the quasipotential at $\rho = 15$ corresponding to $U = 8$ (the green surface), $U = 17.37$ (the blue surface), and $U = 20$ (the red surface). The thick bright red curves are the saddle cycles γ_{\pm} . The dark blue curves are characteristics running from γ_+ and approaching C_{\pm} . The dark red curve is a MAP starting at C_+ and approaching γ_+ . A movie with this figure rotating around the x_3 -axis is available at <https://youtu.be/mzdUD-ngqYs>.

Willing to refine our relatively rough 3D computation and find a more accurate value of the quasipotential on γ_+ with respect to C_+ , we perform 2D computations on the manifold \mathcal{M}_+ consisting of all characteristics going from γ_+ to C_+ using the code `olim2DEquilibLimitCycle.c`. Fig. 7 suggests that \mathcal{M}_+ is close to the 2D manifold consisting of all MAPs from C_+ to γ_+ . So, we neglect the discrepancy between them. We generate 2D radial meshes on \mathcal{M}_+ (see Appendix F) whose coarsened version is shown in Fig. 8(a). The computed quasipotential on \mathcal{M}_+ is shown in Fig. 8(b). We first ran the OLIM on a radial mesh of size 2001×7200 and then repeated the computation on a refined mesh of size 4001×14400 . The radial update factors K_r were 50 and 100 respectively, and the angular update factors K_a were 180 and 360 respectively. For the coarser mesh, the resulting values of the quasipotential on γ_+ varied from 18.19488 to 18.19501 averaging at 18.19495. For the finer mesh, these numbers were, respectively,



(a)



(b)

Figure 8: (a): Radial meshes on the manifold \mathcal{M}_{\pm} consisting of all characteristics going from the saddle cycles γ_{+} (the thick purple curve) and γ_{-} (the thick red curve) to the equilibria C_{\pm} (the large red dots) respectively. (b): The quasipotential computed on \mathcal{M}_{+} .

18.19536, 18.19541, and 18.19536. These results suggest the following estimate for expected escape time from C_+ at $\rho = 15$:

$$\mathbb{E}[\tau_{C_+}] \asymp e^{18.2/\epsilon}. \quad (35)$$

For comparison and a consistency check, we have also found the quasipotential barrier by integrating the geometric action along the MAP going from C_+ to γ_+ . Note that the length of this MAP is infinite. However, the contribution to the geometric action from the integration along its infinite piece lying within an δ -tube around γ_+ tends to zero as $\delta \rightarrow 0$ as the quasipotential is Lipschitz-continuous [4]. Therefore, it suffices to take a finite piece of the MAP starting at C_+ and ending near γ_+ . We took a piece of MAP of length 308.7 and obtained the value of the quasipotential barrier 19.3 which is closer to 18.2 found by the 2D computation rather than to 17.4 found by the 3D one. The result 19.3 is affected by numerical errors in the MAP and by the quadrature error amplified by the large length of the MAP. As ρ increases to $\rho_2 \approx 24.74$, the MAP spirals denser and denser, and integration of the geometric action along it becomes less and less accurate. So, we abandon this consistency check for values of ρ larger than 15.

5.3.2 $\rho = 20$

For $\rho = 20$, we performed a computation in the cube with side 26 centered at C_+ on a $1001 \times 1001 \times 1001$ mesh with $K = 20$. This cube encloses γ_+ . The values of the computed quasipotential on γ_+ range from 6.59 to 6.62 and average at 6.61. The level sets corresponding to $U = 3.3$ and $U = 6.58$ are shown in Fig. 9. A 2D computation on the manifold \mathcal{M}_+ similar to the one described in Section 5.3.1 gave $U(\gamma_+) \in [6.1172, 6.1175]$ with the average at 6.1172. The MAP going from C_+ to γ_+ as well as the characteristics going from γ_+ to C_+ spiral notably denser than their counterparts at $\rho = 15$, and the level sets of the quasipotential are thinner. The saddle cycles are the escape states from the basins of C_\pm to a chaotic region [22] where it is hard to predict for a characteristic which attractor, C_+ or C_- , it will eventually approach. We traced 1000 trajectories starting on the cone Υ_+ (see Table 1) at the points of the form $\mathbf{y}_i := \mathbf{x}_i + 0.002(\mathbf{x}_i - C_+)$ where $\mathbf{x}_i \in \gamma_+$, $i = 1, \dots, 1000$, are equispaced, and recorded whether they converged to C_+ or C_- as $t \rightarrow \infty$: 508 and 492 trajectories converged to C_+ and C_- respectively. Then we subdivided γ_+ into 100 intervals of equal length and used the recorded data to estimate the probability for a trajectory starting at each \mathbf{y}_i corresponding to \mathbf{x}_i in each interval to converge to C_+ . The result is shown in Fig. 10(a). The probabilities for γ_- are obtained by symmetry. Note that a similar calculation for $\rho = 15$ gave the probability distribution depicted in Fig. 10(b): 975 out of 1000 trajectories starting on the analogous points of the cone Υ_+ eventually approached C_- , while 25 returned to C_+ . The uncertainty for where the trajectory of (2) that escapes all level sets of the quasipotential not containing the saddle cycle will eventually go, to C_+ or to C_- , appears where the saddle cycles γ_\pm come close to each other.

Summarizing our findings for $\rho = 20$, we predict that the expected escape time from C_\pm to the chaotic region scales as

$$\mathbb{E}[\tau_{C_+}] \asymp e^{6.1/\epsilon}. \quad (36)$$

5.4 $24.06 \approx \rho_1 < \rho < \rho_2 \approx 24.74$

It was recognized by Lorenz [24] that the strange attractor is an “infinite complex of surfaces”, i.e., a fractal, which is a very complicated geometric object. The addition of small white noise to the Lorenz system regularizes and simplifies its dynamics in the sense that it renders the fine structure of the Lorenz attractor irrelevant and allows for a description of the dynamics in terms of probability measures. Taking this into account, we approximate the strange attractor A_L with

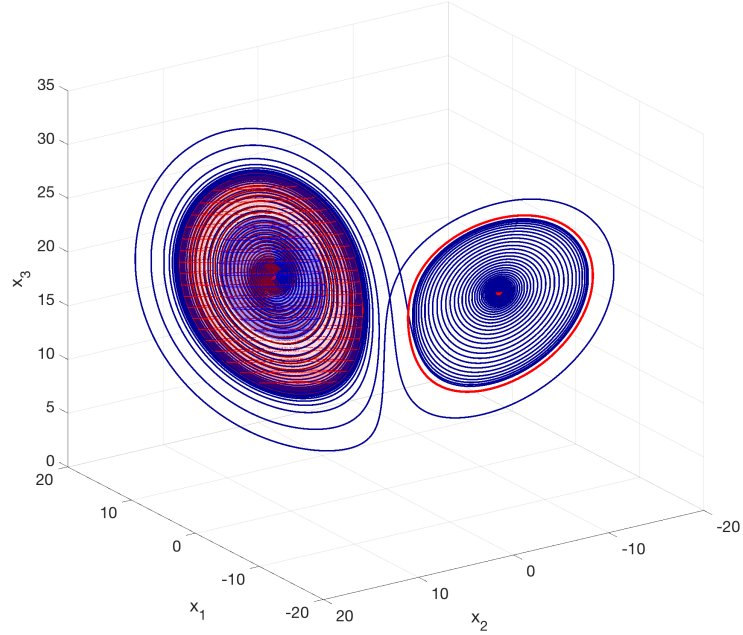


Figure 9: The level sets of the quasipotential at $\rho = 20$ corresponding to $U = 3.3$ (the blue surface), and $U = 6.58$ (the red surface). The thick bright red curves are the saddle cycles γ_{\pm} . The dark blue curves are characteristics going from γ_+ to C_+ and C_- . The dark red curve is a MAP starting at C_+ and approaching γ_+ . A movie with this figure rotating around the x_3 -axis is available at <https://youtu.be/JhBU0-dnos8>.

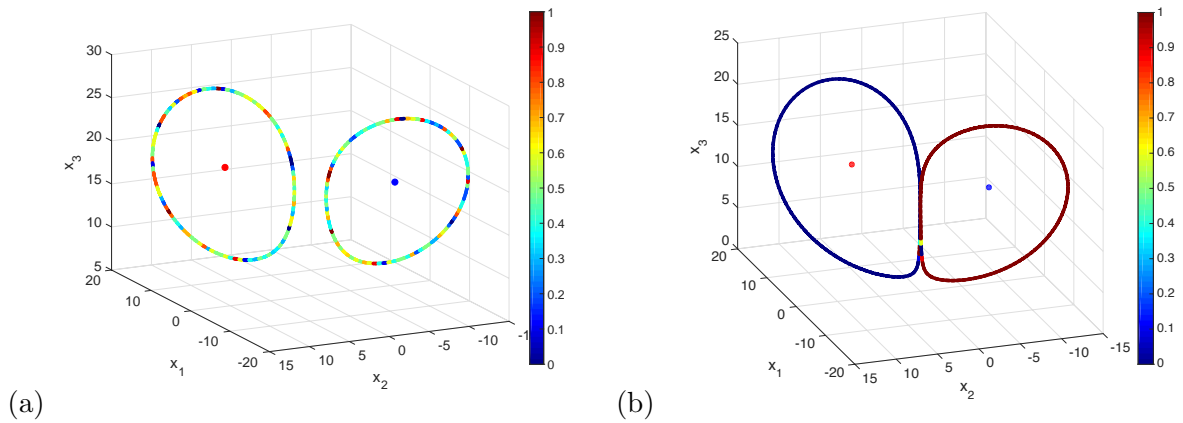


Figure 10: The probability for a trajectory starting on the cones Υ_{\pm} at the point of the form $\mathbf{x} + 0.002(\mathbf{x} - C_{\pm})$ where $\mathbf{x} \in \gamma_{\pm}$ respectively to converge to C_+ . (a): $\rho = 20$. (b): $\rho = 15$.

a union of four manifolds as shown in Fig. 11. These manifolds were obtained using the code `StrangeAttractorMesh.m` in a way similar to the one described in Appendix F. The key component of this construction is finding a trajectory going into the saddle at the origin. We will refer to the inner boundaries of the red and blue manifolds plotted with brown and cyan, respectively, as the eyes Y_+ and Y_- . The union of the red and green boundaries will be called wing W_+ . Similarly, the union of the blue and magenta boundaries forms the wing W_- . In order to understand what is the minimal reasonable value of the parameter ϵ in (2) that makes such an approximation sensible, we have estimated the thickness of the strange attractor at 398 randomly picked points. Details are provided in Appendix G. The thickness map in Fig. 11 indicates that the thickness of A_L does not exceed 10^{-2} wherever it is approximated by a single manifold. Larger values of thickness are found in places where we approximate A_L with two close manifolds. Hence they are just an artifact of our thickness measurement method. The thickness map suggests that $\sqrt{\epsilon}$ in SDE (2) should be at least 10^{-2} , i.e., $\epsilon \gtrsim 10^{-4}$.

We performed a 3D computation of the quasipotential with respect to C_+ aiming at obtaining the overall picture. The computational domain was a box centered at C_+ and embracing the strange attractor. Note that this computation is too rough to give accurate numbers, nevertheless, it captures the geometry of the level sets. The level sets of the computed quasipotential shown in Fig. 12 agree with our expectations: the quasipotential grows until it reaches the strange attractor, it remains nearly constant on it, and then grows fast away from it, mainly along the union of manifolds that extends the strange attractor. Again, we performed a 2D computation on the manifold \mathcal{M}_+ on a radial 6001×7200 mesh with $K_r = 150$ and $K_a = 500$ and found the quasipotential at γ_+ to be equal to 0.03466 (see Fig. 13). For comparison, the 3D computation performed in a cube with size 6 centered at C_+ on a $1001 \times 1001 \times 1001$ mesh with $K = 20$ gave the quasipotential on γ_+ around 0.25 which is more than 7 times larger due to the issues illustrated in Fig. 1. This shows that our reduction to 2D is very important for obtaining accurate quasipotential barriers.

Fig. 11 shows that the quasipotential level sets primarily grow along the edge of the strange attractor while remaining quite thin. This observation suggests two possible transition mechanisms from the strange attractor to C_+ . The first one would start near the eye Y_+ , climb up to γ_+ , and then switch to spiraling toward C_+ . The second one would involve sliding toward γ_+ from the neighborhood of the wing W_- to a region lying between the eye and γ_+ and starting spiraling toward γ_+ and then toward C_+ . Note that a MAP for the second mechanism at $\rho = 24.08$ was found in [40]. Coarsened versions of meshes generated for computing the quasipotential barriers for each of these transition mechanisms are displayed in Fig. 14 (a) and (c) respectively. The “eye” mesh in Fig. 14(a) is lying on the unstable loop-shaped manifold of γ_+ between the γ_+ and Y_+ . Its size is 1501×6000 . The found quasipotential on γ_+ is 0.01543 (see Fig. 14(b)). The “wing+eye” mesh in Fig. 14(c) is defined on the union of the following two manifolds. The wing manifold is defined by trajectories starting near the negative x_3 -semiaxis and bounded by W_+ and a trajectory approaching γ_+ . The second one is the loop-shaped unstable manifold of γ_+ located between γ_+ and Y_+ . The total mesh size is 1501×26001 whose 1501×6000 piece covers the loop. The quasipotential computed on it is shown in Fig. 14(d). Its part corresponding to the loop, naturally, involves significantly smaller values than the one corresponding to the strip around the wing. The quasipotential value on γ_+ for this mesh is 0.01479 which is smaller than the one for the eye mesh.

As we have mentioned above, the strange attractor has a finite width varying roughly from 0 to 10^{-2} . This means that, in order to treat it as a union of four manifolds as shown in Fig. 11 while considering the dynamics according to SDE (2), the parameter ϵ should be chosen at least as large as 10^{-4} . The discussed transition mechanisms from A_L to C_{\pm} are associated with close quasipotential

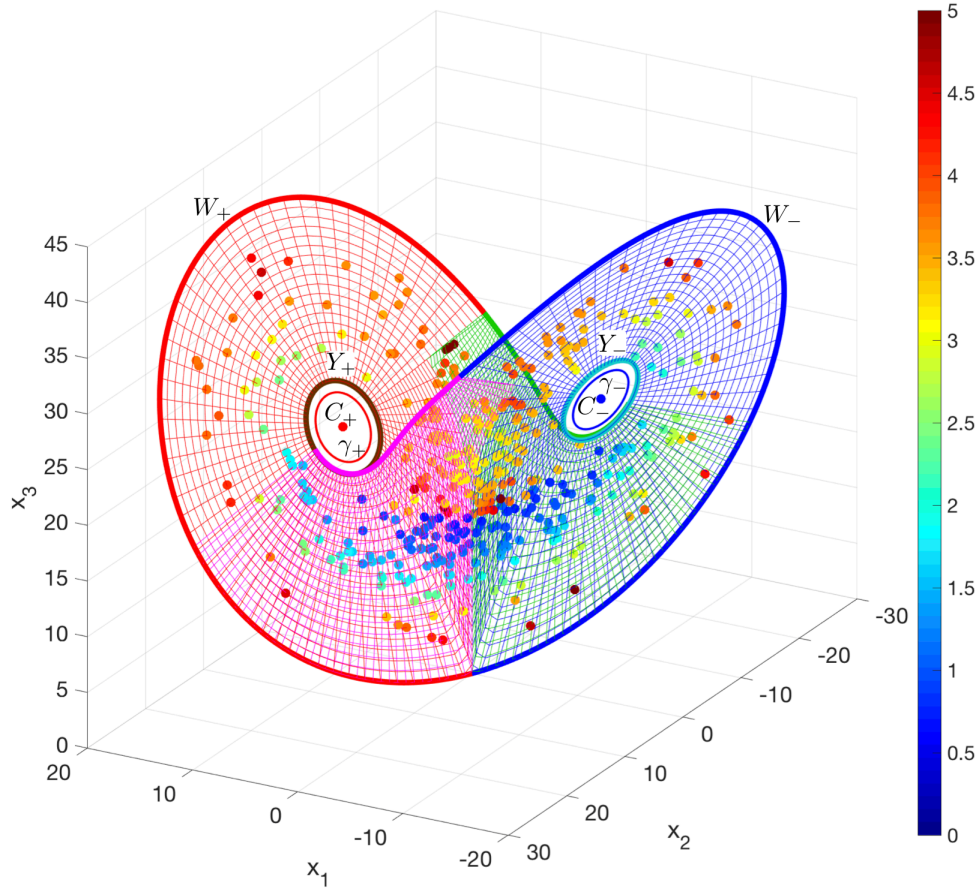


Figure 11: The strange attractor A_L at $\rho = 24.4$ is approximated by a union of four manifolds: red, magenta, blue, and green. The color of the large dots on the manifolds indicate the thickness of the fractal (the Lorenz attractor) at the corresponding locations. The colorbar corresponds to $-\log_{10} w(\mathbf{x})$ where $w(\mathbf{x})$ is the thickness of the fractal near the location \mathbf{x} . Hence dark blue dots indicate thickness $\sim 10^{-1}$, light blue ones $\sim 10^{-2}$, yellow ones $\sim 10^{-3}$, orange ones $\sim 10^{-4}$, and red ones $\sim 10^{-5}$.

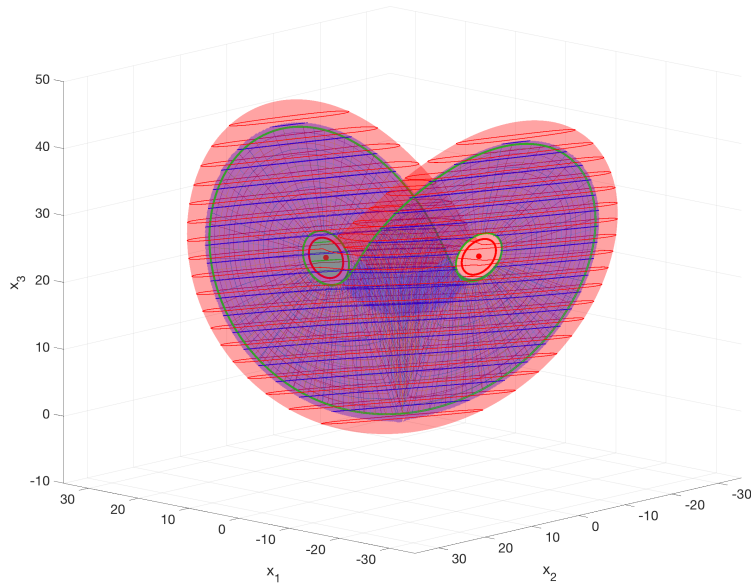


Figure 12: $\rho = 24.4$. The level sets of the quasipotential computed with respect to C_+ . The green surface corresponds to the quasipotential value slightly less than the one at γ_+ . The blue and red ones correspond to $U = 2$ and $U = 20$ respectively. The strange attractor is depicted with a mesh visible inside the blue and red surfaces. A movie with this figure rotating around the x_3 -axis is available at <https://youtu.be/ELqkeb8M1fg>.

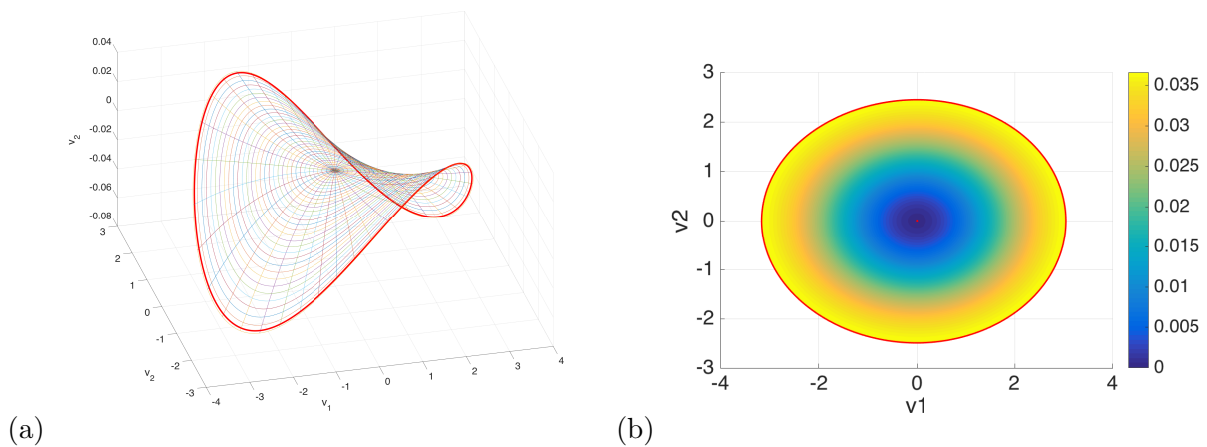


Figure 13: (a): A coarsened radial mesh on the manifold \mathcal{M}_+ at $\rho = 24.4$. The coordinate system is associated with the directions of eigenvectors of the quasipotential matrix for the Jacobian evaluated at C_+ . (b): The quasipotential computed on this mesh.

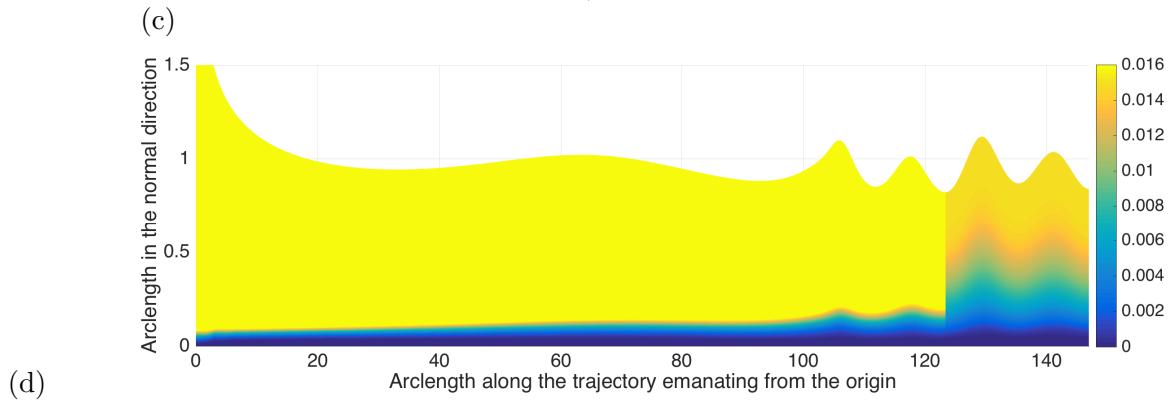
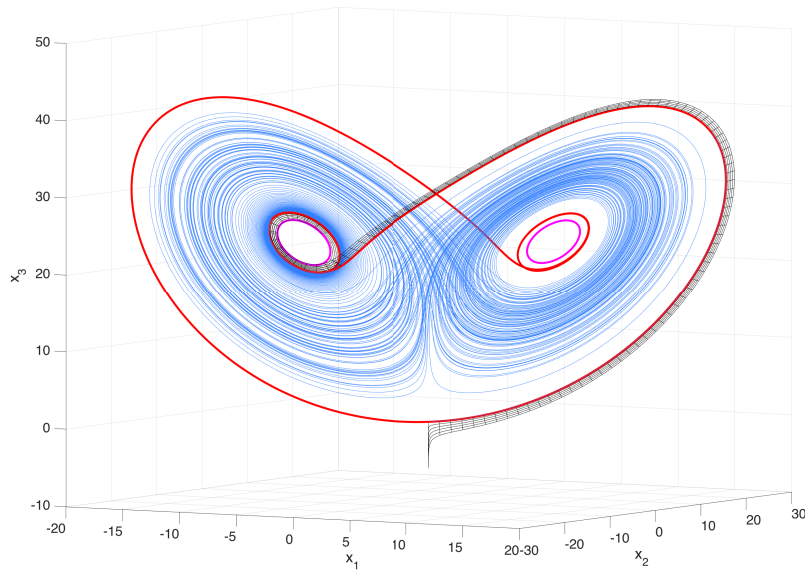
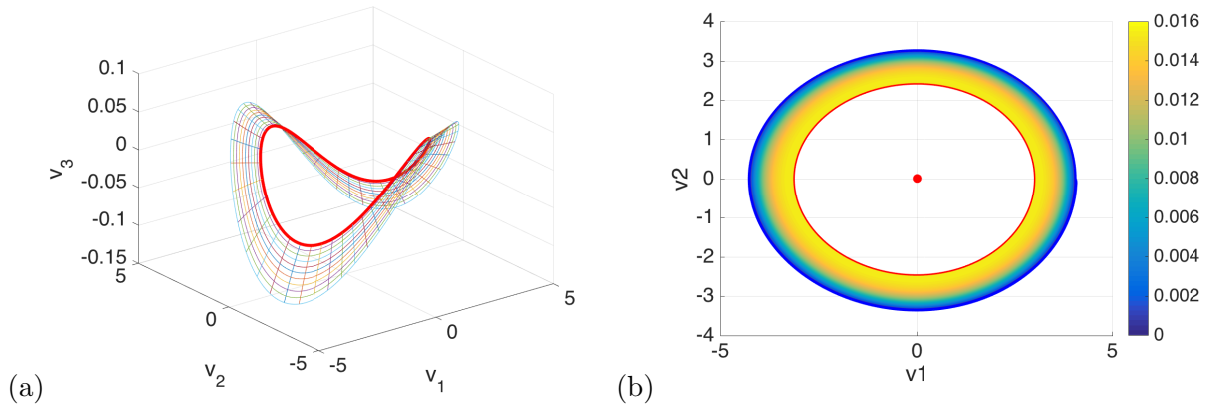


Figure 14: $\rho = 24.4$. (a): A coarsened version of the “eye” mesh. The coordinate axes \mathbf{v}_i , $i = 1, 2, 3$ are chosen along the eigenvectors of the quasipotential matrix Q of the linearized near C_+ vector field. (b): The quasipotential computed on the “eye” mesh. (c): A coarsened version of the “wing+eye” mesh. (d): The quasipotential computed on the “wing+eye” mesh. The arclength values less and greater than approximately 125 correspond to the “wing” and “eye” meshes respectively. The discontinuity along the line where these meshes are glued is caused by the behavior of MAPs. The lightest yellow region of the plot corresponds to values of the quasipotential exceeding the maximal value 0.016 on the colorbar.

barriers: the difference between them is about $5 \cdot 10^{-4}$. Therefore, in order to determine which transition mechanism is dominant for $\epsilon \sim 10^{-4}$, one needs to compute the pre-exponential factors of the corresponding transition rates. Estimation of these prefactors is beyond the scope of the present work. We leave the development of numerical methods for their evaluation for the future.

We summarize the found quasipotential barriers in Table 2.

Table 2: Quasipotential barriers for stochastic Lorenz’63 (2) at $\sigma = 10$, $\beta = 8/3$, and a set of values of ρ .

ρ	Attractor	Escape state	Barrier
12	C_+	The origin	19.5
15	C_+	γ_+	18.2
20	C_+	γ_+	6.1
24.4	C_+	γ_+	0.0247
24.4	A_L	γ_+	0.0154 (“eye”)
24.4	A_L	γ_+	0.0148 (“wing+eye”)

5.5 Perspectives and challenges for large ρ

Our numerical experiments show that the level sets of the quasipotential thin out and the diameter of the strange attractor increases as ρ grows (Fig. 15). On one hand, this creates an underresolution problem for 3D computations as mesh planes cannot be aligned with the level sets of the quasipotential because they are not flat. Handling this issue by means of mesh refinement is limited by computer’s memory. For example, for $\rho = 100.75$ where two attracting limit cycles exist, the minimal level set of the quasipotential computed with respect to one of these cycles and enclosing the other one is thinner than the mesh step at some places.

On the other hand, thinning out of the level sets allows us to use 2D computations provided that we have an insight about possible transition mechanisms as we have had for $\rho = 24.4$. This insight for larger values of ρ can be gained from a 3D computation conducted not in a box but on a specially designed mesh.

6 Conclusions

We have developed a methodology for computing the quasipotential and finding quasipotential barriers for highly dissipative and possibly chaotic 3D dynamical systems perturbed by small white noise. The proposed approach combines 3D computations on regular rectangular meshes with, if relevant, dimensional reduction techniques and 2D computations on radial meshes. This methodology has been developed on and applied to stochastic Lorenz’63 with $\sigma = 10$, $\beta = 8/3$, and a number of values of ρ ranging from 0.5 to 24.4.

We have shown that, as ρ increases, the level sets of the quasipotential thin out and the ratio of magnitudes of the rotational and potential components grows dramatically. On one hand, these facts render the numbers produced by 3D computations progressively less accurate. On the other hand, the manifolds consisting of characteristics going from escape states to attractors and those consisting of MAPs running the other way around become very close to each other. This observation motivated us to approximate the manifolds formed by the MAPs with those consisting of the characteristics.

We have developed a technique for generating radial meshes on manifolds consisting of such characteristics and tested our 2D OLIM quasipotential solver on an ad hoc system where the magnitude of the rotational component exceeds that of the potential one by the factor at least as large as 10^3 , approximately as it is for $\rho = 24.4$ in (2). The least squares fit for this example has given a superquadratic convergence and small normalized maximal absolute errors on practical mesh sizes.

Using a combination of 3D and 2D computations, we found quasipotential barriers for the escapes from the basins of C_{\pm} at $\rho = 12, 15, 20$, and 24.4 . Furthermore, we estimated quasipotential barriers for the escape from the basin of the Lorenz attractor at $\rho = 24.4$ via two escape mechanisms. These barriers for 24.4 are close to each other: the difference between them is of the same order of magnitude as the minimal value of ϵ that makes traversing between different sheets of the Lorenz attractor easy. Therefore, estimates for the pre-exponential factors for these escape rates are necessary in order to determine which transition mechanism is dominant. We have left the development of techniques for computing these prefactors for the future.

An important advantage of computing the quasipotential in 3D is that it allows us to visualize the stochastic dynamics. Plots of quasipotential level sets reveal the hierarchy of regions of the phase space reachable by the system perturbed by small white noise on different timescales. In particular, the visualization of the level sets of the quasipotential at $\rho = 24.4$ suggested us to consider and compare two possible transition mechanisms between the strange attractor and the stable equilibria.

Our C and Matlab programs developed for the application to Lorenz'63 are posted on M. Cameron's web site [5] (see the package `Qpot4Lorenz63.zip`) and on GitHub [6].

The numerical techniques developed in this work can be used for the quasipotential analysis of certain classes of other 2D and 3D SDEs. The dimensional reduction to 2D can be beneficial for any 3D SDEs where the quasipotential with respect to an attractor grows primarily along some 2D manifold. The use of radial meshes can dramatically improve the accuracy of found quasipotential thresholds in the case if the attractor is a stable spiral point and, perhaps, the transition state is an unstable limit cycle.

The application to the Lorenz'63 model allows us to see the limitations of the 3D quasipotential solver: the growth of required computational domains together with thinning out of the level sets results in underresolving the latter even with the use of 1001^3 mesh sizes. This motivates the directions of the future research associated with (i) combining the 3D OLIMs with techniques for generating a 3D mesh adapted for the geometry of the problem and (ii) advancing the techniques for learning 2D manifolds near which the stochastic dynamics are effectively focused.

Acknowledgements

We thank Dr. E. S. Kurkina for inspiring discussions on the Lorenz'63 system and sharing numerical techniques for plotting bifurcational diagrams and finding unstable limit cycles. We are also grateful to Prof. James Yorke and Prof. Kevin Lin for valuable advice regarding preparation of this manuscript. This work is partially supported by NSF grant DMS1554907.

A Derivation of some equations in Section 2.

A.1 The geometric action (9)

Let $\phi : [T_0, T_1] \rightarrow \mathbb{R}^d$ be a path with the endpoints $\phi(T_0) \in A$ and $\phi(T_1) = \mathbf{x}$. Expanding the squared norm in Eq. (8) and using the inequality

$$\|\dot{\phi}\|^2 + \|\mathbf{b}(\phi)\|^2 \geq 2\|\dot{\phi}\|\|\mathbf{b}(\phi)\|$$

we obtain

$$S_{T_0, T_1}(\phi) \geq \int_{T_0}^{T_1} \left(\|\mathbf{b}(\phi)\|\|\dot{\phi}\| - \mathbf{b}(\phi) \cdot \dot{\phi} \right) dt. \quad (37)$$

The equality takes place if and only if $\|\mathbf{b}(\phi)\| = \|\dot{\phi}\|$. Since we are taking the infimum of $S_{T_0, T_1}(\phi)$ in particular with respect to T_0 and T_1 , we choose the parametrization of ϕ so that $\|\mathbf{b}(\phi)\| = \|\dot{\phi}\|$ and change T_0 and T_1 accordingly. Note that T_0 and T_1 are allowed to be $-\infty$ and $+\infty$ respectively. Next, we observe that the integral in the right-hand side of Eq. (37) is invariant under reparametrization of the path ϕ . We denote the path ϕ reparametrized by its arclength by ψ and obtain Eq. (9).

A.2 The Hamilton-Jacobi equation (11) for the quasipotential and equation (13) for the MAP

Let the path ψ parametrized according to its arclength (i.e., $\|\psi'\| = 1$) be the minimizer of the geometric action (9) among all absolutely continuous paths with one endpoint at \mathbf{x} and the other one at A . Let us pick a small number $\delta > 0$. Using Bellman's optimality principle [2] and Taylor expansion of U , we obtain

$$\begin{aligned} U(\mathbf{x}) &= \inf_{\|\psi'\|=1} \left\{ \int_0^\delta (\|\mathbf{b}(\psi)\| - \mathbf{b}(\psi) \cdot \psi') ds + U \left(\mathbf{x} - \int_0^\delta \psi' ds \right) \right\} \\ &= \inf_{\|\psi'\|=1} \left\{ \delta (\|\mathbf{b}(\psi)\| - \mathbf{b}(\psi) \cdot \psi' - \nabla U(\mathbf{x}) \cdot \psi') + U(\mathbf{x}) + O(\delta^2) \right\}. \end{aligned}$$

Canceling $U(\mathbf{x})$ on both sides and dividing by δ we get

$$0 = \inf_{\|\psi'\|=1} \left\{ \|\mathbf{b}(\psi)\| - \mathbf{b}(\psi) \cdot \psi' - \nabla U(\mathbf{x}) \cdot \psi' + O(\delta) \right\}.$$

Taking the limit as $\delta \rightarrow 0$, we obtain

$$\inf_{\|\psi'\|=1} \left\{ \|\mathbf{b}(\mathbf{x})\| - (\mathbf{b}(\mathbf{x}) + \nabla U(\mathbf{x})) \cdot \psi' \right\} = 0. \quad (38)$$

The infimum is attained when the term $(\mathbf{b}(\mathbf{x}) + \nabla U(\mathbf{x})) \cdot \psi'$ is maximal, i.e., when

$$\psi' = \frac{\mathbf{b}(\mathbf{x}) + \nabla U(\mathbf{x})}{\|\mathbf{b}(\mathbf{x}) + \nabla U(\mathbf{x})\|}. \quad (39)$$

Observing that \mathbf{x} is the point of the path ψ at which ψ' is evaluated, we see that (39) coincides with equation (13). Plugging (39) into (38), we get

$$\|\mathbf{b}(\mathbf{x})\| = \|\mathbf{b}(\mathbf{x}) + \nabla U(\mathbf{x})\|. \quad (40)$$

Taking squares of both sides of Eq. (38), canceling $\|\mathbf{b}(\mathbf{x})\|^2$, and dividing by 2, we obtain the desired Hamilton-Jacobi equation (11):

$$\frac{1}{2} \|\nabla U(\mathbf{x})\|^2 + \mathbf{b}(\mathbf{x}) \cdot \nabla U(\mathbf{x}) = 0.$$

B The dynamics of the Lorenz system (16)

Let us fix the parameters $\sigma = 10$ and $\beta = 8/3$. As ρ grows from zero to infinity, the dynamics of (16) go through a number of bifurcations [22, 31, 32, 33].

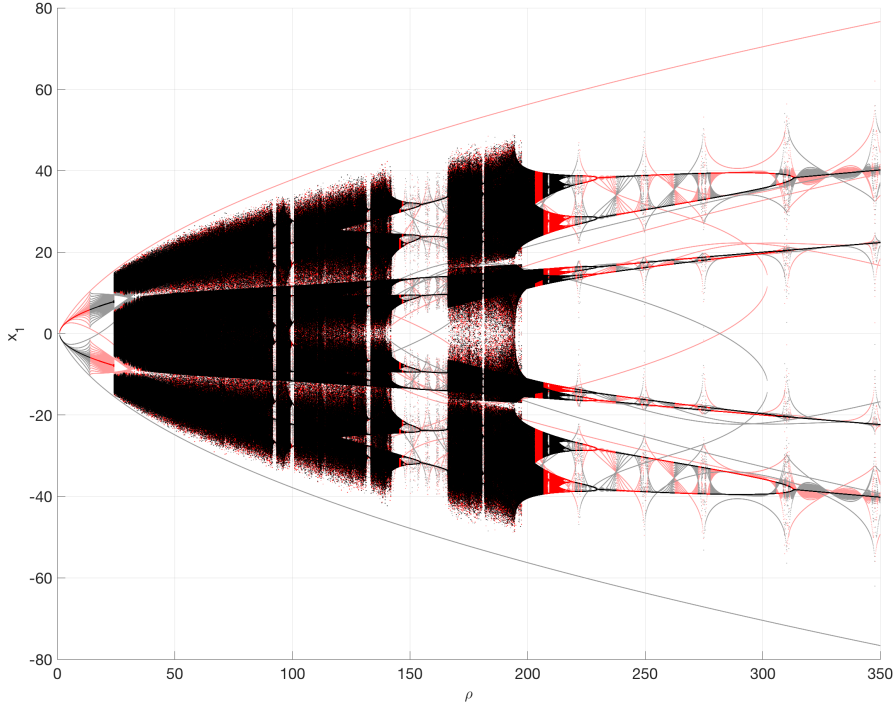


Figure 15: Consider the characteristics of (16) emanating from the origin along the directions ξ and $-\xi$ and traced for the time interval $0 \leq t \leq 200$. The x_1 -components of their intersections with the horizontal plane passing through the equilibria C_{\pm} are plotted for $1 \leq \rho \leq 350$ with pink and grey dots respectively. Then each characteristic is continued to be traced for $200 \leq t \leq 400$. The resulted x_1 components of their intersections with the same plane are marked with red and black respectively. The dashed green vertical lines correspond to the critical values of ρ : $\rho_0 \approx 13.926$, $\rho_1 \approx 24.06$, and $\rho_2 \approx 24.74$.

- For all $0 < \rho < \infty$, the origin is a fixed point of (16). It is the only equilibrium for $0 < \rho < 1$, and it is globally attracting. At $\rho = 1$, a supercritical pitchfork bifurcation occurs transforming the origin into a Morse index one saddle and giving birth to two equilibria

$$C_{\pm} = \left(\pm\sqrt{\beta(\rho-1)}, \pm\sqrt{\beta(\rho-1)}, \rho-1 \right). \quad (41)$$

They remain asymptotically stable for $1 < \rho < \rho_2 \approx 24.74$. The unstable manifold of (16)

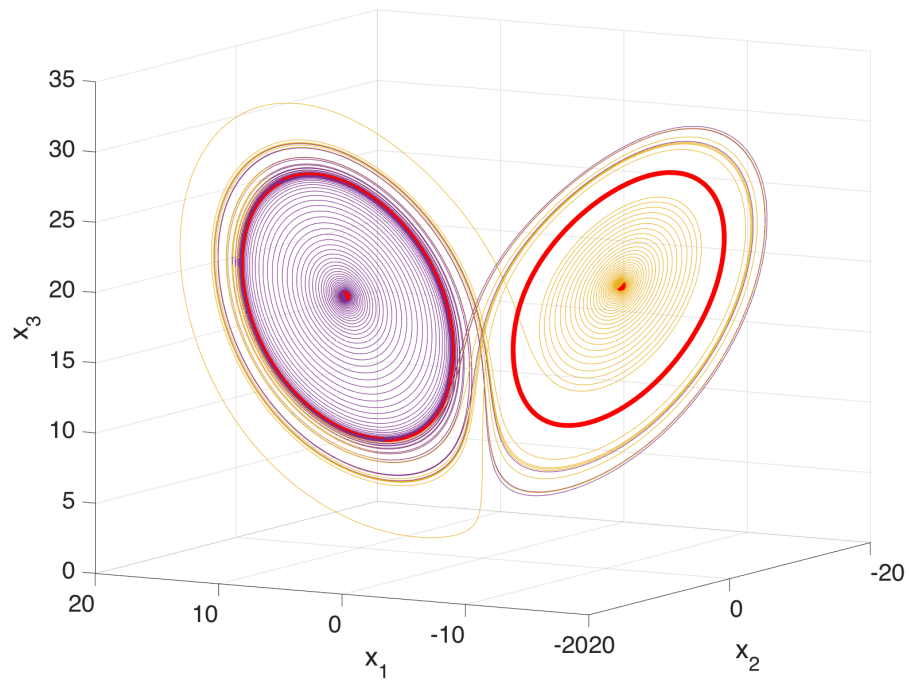


Figure 16: (a): An example of two characteristics at $\rho = 20$ starting at two close points lying near γ_+ on the cone with vertex at C_+ and consisting of all rays passing through γ_+ and eventually diverging and approaching different equilibria.

linearized near the saddle at the origin for $1 < \rho < \infty$ is the span of the vector

$$\xi = \begin{bmatrix} \frac{\sigma}{2} + \sqrt{\left(\frac{\sigma+1}{2}\right)^2 + \sigma(\rho-1)} \\ \frac{\sigma-1}{2} \\ 0 \end{bmatrix}. \quad (42)$$

To delineate the evolution of the dynamics of (16) as ρ grows from 1 to infinity, we have plotted the bifurcation diagram displayed in Fig. 15. For each ρ from 1.05 to 349.95 with step 0.1, we traced the trajectory starting at $10^{-2}\xi$ for time $0 \leq t \leq 200$ and recorded its points of intersection with the plane

$$\alpha = \{\mathbf{x} \mid x_3 = \rho - 1\}$$

passing through the equilibria C_{\pm} . The x_1 -components of these intersects are shown with pink dots in the (ρ, x_1) -plane. The time interval $0 \leq t \leq 200$ is large enough for this trajectory to approach an attractor. Then, in order to depict x_1 -components of the intersection of the attractor with the plane α , we continued tracing the trajectory for $200 \leq t \leq 400$ and plotted the x_1 components of its intersects with α with red dots. The corresponding sets of points for the trajectory starting at $-10^{-2}\xi$ are obtained using the aforementioned symmetry of (16). They are plotted with grey and black dots respectively. This procedure is implemented in the Matlab code `lorenz_diagram.m`.

- For $1 < \rho < \rho_0 \approx 13.926$, the characteristics emanating from the saddle at the origin along the directions ξ and $-\xi$ approach, respectively, C_+ and C_- without crossing the plane $x_1 = 0$ (see Fig. 15).
- The interval $13.926 \approx \rho_0 < \rho < \rho_2 \approx 24.74$ is marked by the existence of the saddle limit cycles γ_+ and γ_- surrounding C_+ and C_- respectively. The equilibria C_{\pm} remain the only attractors for $\rho_0 < \rho < \rho_1 \approx 24.06$. At $\rho = \rho_0$, there exist homoclinic orbits emanating from the origin and approaching it as $t \rightarrow \infty$. For all $\rho_0 < \rho < \rho_1$, the characteristics emanating from the origin along the directions ξ and $-\xi$ go approximately half-way around the limit cycles, cross the plane $x_1 = 0$, and approach C_- and C_+ respectively (see Fig. 15). As ρ grows within this interval, there develops a phenomenon called *preturbulence* [22], characterized by chaotic behavior and divergence of close characteristics in a region surrounding γ_{\pm} . Let Υ_+ be a cone consisting of all rays starting at C_+ and crossing γ_+ , i.e.,

$$\Upsilon_+ := \{C_+ + t(\mathbf{x} - C_+) \mid t \geq 0, \mathbf{x} \in \gamma_+\}. \quad (43)$$

Characteristics starting on Υ_+ near and outside γ_+ perform more and more revolutions around C_+ and C_- prior they settle to spiraling near one of the stable equilibria. Moreover, as ρ tends to ρ_1 , it is getting progressively harder and finally impossible to predict using double-precision arithmetic which equilibrium such a characteristic will eventually approach. An example of two characteristics for $\rho = 20$ starting at two close points near γ_+ on the cone Υ_+ and eventually approaching different equilibria is shown in Fig. 16. At $\rho = \rho_1$, the characteristics emanating from the origin along the directions ξ and $-\xi$ approach γ_- and γ_+ respectively. This gives birth to a strange attractor a.k.a. the Lorenz attractor. We will denote it by A_L .

- For $24.06 \approx \rho_1 < \rho < \rho_2 \approx 24.74$, there are three attractors: the strange attractor A_L , and the asymptotically stable equilibria C_{\pm} . The characteristics emanating from the origin along $\pm\xi$ miss the saddle cycles γ_{\mp} respectively and start spiraling away from them. γ_{\pm} lie on the

boundaries of the basins of C_{\pm} respectively and, as we show in Section 5.4, play roles of the escape states. At $\rho = \rho_2$, the saddle cycles γ_{\pm} shrink to the corresponding equilibria C_{\pm} rendering them unstable, i.e., a subcritical Hopf bifurcation takes place.

- For $24.74 \approx \rho_2 < \rho < \infty$, the dynamics are complicated as can be inferred from Fig. 15. A_L is the only attractor for some open interval of ρ starting at ρ_2 (Fig. 15). It exists for a union of intervals of ρ stretching up to approximately $\rho = 215.364$ [31]. The interval $\rho_2 < \rho \lesssim 215.364$ is cut through by a number of windows of periodicity where there exist attracting limit cycles. The largest of them is $145 \lesssim \rho \lesssim 166$. Other windows are seen around $\rho = 93$, $\rho = 100$, $\rho = 133$, and $\rho = 181.5$. Zooming in, we can spot more windows of periodicity (see Fig. 15) and reveal cascades of period doublings marking the Feigenbaum scenarios of transition to chaos. The final doubling period interval $215.364 \lesssim \rho \lesssim 313$ [31] is clearly visible in Fig. 15. Near $\rho = 313$, two symmetric attracting limit cycles merge into one resulting in the final limit cycle that remains the only attractor for all larger values of ρ .

C The KKT conditions for the simplex update

The Lagrange function for the constrained minimization problem (19)–(20) is

$$\mathcal{L}(\lambda, \mu) = U_{\lambda} + \mathcal{Q}_M(\mathbf{x}_{\lambda}, \mathbf{x}) - \mu_1 \lambda_1 - \mu_2 \lambda_2 - \mu_3 (1 - \lambda_1 - \lambda_2), \quad (44)$$

where $\lambda = [\lambda_1, \lambda_2]$ and $\mu = [\mu_1, \mu_2, \mu_3]$. For brevity, we denote the function to be minimized by f :

$$f(\lambda) := U_{\lambda} + \mathcal{Q}_M(\mathbf{x}_{\lambda}, \mathbf{x}).$$

The KKT optimality conditions applied to (44) are

$$\nabla_{\lambda} \mathcal{L}(\lambda, \mu) = \nabla f(\lambda) - \mu_1 \begin{bmatrix} 1 \\ 0 \end{bmatrix} - \mu_2 \begin{bmatrix} 0 \\ 1 \end{bmatrix} - \mu_3 \begin{bmatrix} -1 \\ -1 \end{bmatrix} = \begin{bmatrix} 0 \\ 0 \end{bmatrix} \quad (45)$$

$$\mu_1 \geq 0, \quad \mu_2 \geq 0, \quad \mu_3 \geq 0, \quad (46)$$

$$\lambda_1 \geq 0, \quad \lambda_2 \geq 0, \quad 1 - \lambda_1 - \lambda_2 \geq 0, \quad (47)$$

$$\lambda_1 \mu_1 = 0, \quad \lambda_2 \mu_2 = 0, \quad (1 - \lambda_1 - \lambda_2) \mu_3 = 0. \quad (48)$$

Let us check whether the initial guess $\lambda = [\lambda^*, 0]$ where λ^* is the minimizer of f on $[\lambda_1, 0]$, $0 < \lambda_1 < 1$, corresponding to the line segment $[\mathbf{x}_0, \mathbf{x}_1]$, satisfies the KKT conditions (45)–(48). Condition (48) with $\lambda_1 = \lambda^* \in (0, 1)$ and $\lambda_2 = 0$ implies that $\mu_1 = \mu_3 = 0$. Therefore, the first component in (45) is zero as

$$\frac{\partial}{\partial \lambda_1} f(\lambda^*, 0) = 0. \quad (49)$$

The second component of (45) must be also zero, hence

$$\frac{\partial}{\partial \lambda_2} f(\lambda^*, 0) - \mu_2 = 0. \quad (50)$$

Condition (46) demands that $\mu_2 \geq 0$. Hence, $\lambda = [\lambda^*, 0]$ is a solution of the constrained minimization problem (19)–(20) if

$$\mu_2 = \frac{\partial}{\partial \lambda_2} f(\lambda^*, 0) \geq 0, \quad (51)$$

i.e., if equation (21) holds. In this case, we reject the simplex update. Otherwise, we proceed with solving the minimization problem (19)–(20).

D Quasipotential decomposition for linear SDEs

In this Appendix, we explain how one can find the quasipotential for linear SDEs for which the origin is an asymptotically stable equilibrium. This is useful for initializing the OLIMs near asymptotically stable equilibria and for estimating the ratio of the magnitudes of the rotational and potential components of the vector field.

Let J be a $d \times d$ matrix with all eigenvalues having negative real parts. In this work, J is the Jacobian matrix of the vector field \mathbf{b} evaluated at an asymptotically stable equilibrium \mathbf{x}^* of $\dot{\mathbf{x}} = \mathbf{b}(\mathbf{x})$. We consider the linear SDE for the variable $\mathbf{y} := \mathbf{x} - \mathbf{x}^*$:

$$d\mathbf{y} = J\mathbf{y}dt + \sqrt{\epsilon}d\mathbf{w}. \quad (52)$$

The problem of finding the quasipotential decomposition for the vector field $J\mathbf{y}$ reduces to the problem of finding a symmetric positive definite matrix Q such that [8, 9]

$$\mathbf{y}^\top Q(J + Q)\mathbf{y} = 0 \quad \text{for all } \mathbf{y} \in \mathbb{R}^d. \quad (53)$$

The matrices Q and $L := J + Q$ are called the *quasipotential matrix* and the *rotational matrix* respectively. Condition (53) is equivalent to the requirement that the matrix $Q(J + Q)$ is antisymmetric, i.e., $Q(J + Q) + (J + Q)^\top Q = 0$. The last equation for Q is reducible to a Sylvester equation for Q^{-1} and has a unique positive definite solution that can be found using the Bartels-Stewart algorithm implemented in Matlab in the command `sylvester` (see [38] for details).

To make our quasipotential solver for the Lorenz system self-contained and facilitate experiments with various values of ρ , we have developed a C code `LinLorenz.c` for finding the quasipotential decomposition for the Lorenz system linearized near its asymptotically stable equilibria. The quasipotential decomposition is found by an algorithm similar to Bartels-Stewart but simplified and customized for Lorenz'63. A description of it is linked to the provided software package [5].

Once the quasipotential decomposition for a linearized system is available, one can obtain an estimate for the ratio $\Xi(\mathbf{x})$ of the magnitudes of the rotational and potential components near asymptotically stable equilibria:

$$\Xi \lesssim \max_{\|\mathbf{y}\|=1} \frac{\|L\mathbf{y}\|}{\|Q\mathbf{y}\|}. \quad (54)$$

The graph of the right-hand side of (54) with J been the Jacobian matrix evaluated at C_+ of (16) is plotted in Fig. 2 for the range $1 < \rho < \rho_2 \approx 24.74$.

E Proof of Lemma 4.1

Proof. First we prove that the manifold \mathcal{M}' consisting of MAPs going from the attractor A to the curve γ lies in the sublevel set \mathcal{V}_a . Let ψ be a MAP going from A to γ . Since \mathcal{V}_a completely lies in the basin of A , the quasipotential strictly increases along the MAP. Therefore, for any \mathbf{y} lying on the path ψ , $U(\mathbf{y}) \leq a$ which means that $\psi \subset \mathcal{V}_a$. Since this is true for all such MAPs, $\mathcal{M}' \subset \mathcal{V}_a$.

Now let us prove that the manifold \mathcal{M} consisting of all characteristics starting at γ and running to A lies in \mathcal{V}_a . We proceed from converse. Suppose a characteristic starting at γ and going to A leaves \mathcal{V}_a at a point \mathbf{x}_0 and reenters \mathcal{V}_a at a point \mathbf{x}_1 after that. Let \mathbf{y} be a point of this characteristic located between \mathbf{x}_0 and \mathbf{x}_1 . Since the motion of the characteristic contributes nothing to the Freidlin-Wentzell action (8), $U(\mathbf{y}) = U(\mathbf{x}_0) = a$. This contradicts to the assumption that $\mathbf{y} \notin \mathcal{V}_a$. Therefore, the characteristic must completely lie in \mathcal{V}_a . Since this argument applies all characteristics constituting \mathcal{M} , we conclude that $\mathcal{M} \subset \mathcal{V}_a$. \square

F Building radial meshes

Suppose we would like to build a radial mesh on a 2D manifold formed by characteristics of $\dot{\mathbf{x}} = \mathbf{b}(\mathbf{x})$ going from an unstable limit cycle γ to an asymptotically stable spiral point \mathbf{x}^* . First, we pick a set of points \mathbf{x}^k , $k = 0, 1, \dots, N_a - 1$, equispaced along γ . For each point \mathbf{x}^k , we define a plane α^k passing through \mathbf{x}^* and \mathbf{x}^k whose normal \mathbf{a}^k lies in the plane spanned by $\mathbf{b}(\mathbf{x}^k)$ and $\mathbf{x}^k - \mathbf{x}^*$.

Then, we trace a trajectory $\mathbf{y}(t)$ starting near γ and ending upon reaching a δ -ball centered at \mathbf{x}^* where δ is a small number. Let $\mathbf{y}_1, \dots, \mathbf{y}_n$ be the set of intersects of $\mathbf{y}(t)$ with the plane α^0 at which the sign of $(\mathbf{y}(t) - \mathbf{x}^0)^\top \mathbf{a}^0$ changes from “-” to “+”. Adding \mathbf{x}^0 and \mathbf{x}^* to this set and interpolating, we get a curve lying in α_0 and connecting γ and \mathbf{x}^* . We define a set of points $\{\mathbf{z}_i^0\}_{i=0}^{N_r-1}$ uniformly distributed along this curve such that $\mathbf{z}_0^0 \equiv \mathbf{x}^*$ and $\mathbf{z}_{N_r-1}^0 \equiv \mathbf{x}^0$.

Next, for $k = 0, 1, 2, \dots, N_a - 2$, we trace the trajectories starting at \mathbf{z}_i^k , $i = 1, \dots, N_r - 2$, and terminate them as soon as they reach the plane α_{k+1} . As above, we add \mathbf{x}_{k+1} and \mathbf{x}^* to these terminal points, interpolate them, and pick a set of points \mathbf{z}_i^{k+1} , $i = 0, \dots, N_r - 1$, uniformly distributed along the interpolant and such that $\mathbf{z}_0^{k+1} \equiv \mathbf{x}^*$ and $\mathbf{z}_{N_r-1}^{k+1} \equiv \mathbf{x}^{k+1}$. As a result, we obtain the radial mesh

$$\{\mathbf{z}_i^k \mid 0 \leq i \leq N_r - 1, 0 \leq k \leq N_a - 1\}.$$

This procedure is implemented in the Matlab code `make2Dmesh.m` in `Qpot4Lorenz63.zip` [5].

Similar methodologies have been used to construct radial meshes between two simple closed curves and between two given segments of two distinct characteristics.

G Estimating the width of the Lorenz attractor

Let \mathbf{x} be a point lying on the Lorenz attractor A_L and let α be the plane passing through \mathbf{x} and normal to $\mathbf{b}(\mathbf{x})$ where \mathbf{b} is the Lorenz vector field, i.e.,

$$\alpha := \{\mathbf{z} \in \mathbb{R}^3 \mid (\mathbf{z} - \mathbf{x})^\top \mathbf{b}(\mathbf{x}) = 0\}.$$

We trace a trajectory $\mathbf{y}(t)$ starting at \mathbf{x} for time 10^4 and record the points \mathbf{y}_i , $1 \leq i \leq N$, at which the sign of $(\mathbf{y}(t) - \mathbf{x})^\top \mathbf{b}(\mathbf{x})$ switches from “-” to “+”. We set up a Cartesian coordinate system (η_1, η_2) in the plane α with the origin at $\mathbf{y}_1 \equiv \mathbf{x}$ and find the coordinates of the recorded points \mathbf{y}_i : $\mathbf{y}_i \equiv (\eta_1^i, \eta_2^i)$. We pick a square $S := [-0.25 \leq \eta_1 \leq 0.25] \times [-0.25 \leq \eta_2 \leq 0.25]$ in this plane and select the subset $I \subset \{1, \dots, N\}$ such that the points \mathbf{y}_i , $i \in I$, lie in S . Visualizing the set \mathbf{y}_i , $i \in I$, and zooming in if necessary, we see that they are arranged near two almost parallel lines (see Fig. 17). The least squares fit to this set of points with a linear function $\eta_2 = a\eta_1 + b$ gives a line dividing it into two subsets:

$$I_1 = \{i \in I \mid \eta_2^i < a\eta_1^i + b\} \quad \text{and} \\ I_2 = \{i \in I \mid \eta_2^i > a\eta_1^i + b\}.$$

Next, we find linear least squares fits $\eta_2 = a_1\eta_1 + b_1$ and $\eta_2 = a_2\eta_1 + b_2$ for the subsets of \mathbf{y}_i corresponding to I_1 and I_2 , respectively. One of these linear functions must pass very close to the origin because \mathbf{x} lies near one of these lines, hence either b_1 or b_2 is very close to zero in comparison with the other one. Assume that $|b_2| \ll |b_1|$. If this is the other way around, we swap the notations. Also, these lines are almost parallel, hence a_1 and a_2 are very close. Finally, we find a line orthogonal to $\eta_2 = a_1\eta_1 + b_1$ and passing through the origin: $\eta_2 = -a_1^{-1}\eta_1$. Then the thickness of A_L near \mathbf{x}

is approximately equal to the distance between the origin and the intersect of $\eta_2 = -a_1^{-1}\eta_1$ and $\eta_2 = a_1\eta_1 + b_1$. This technique is implemented in the Matlab program `thickness.m` [5, 6].

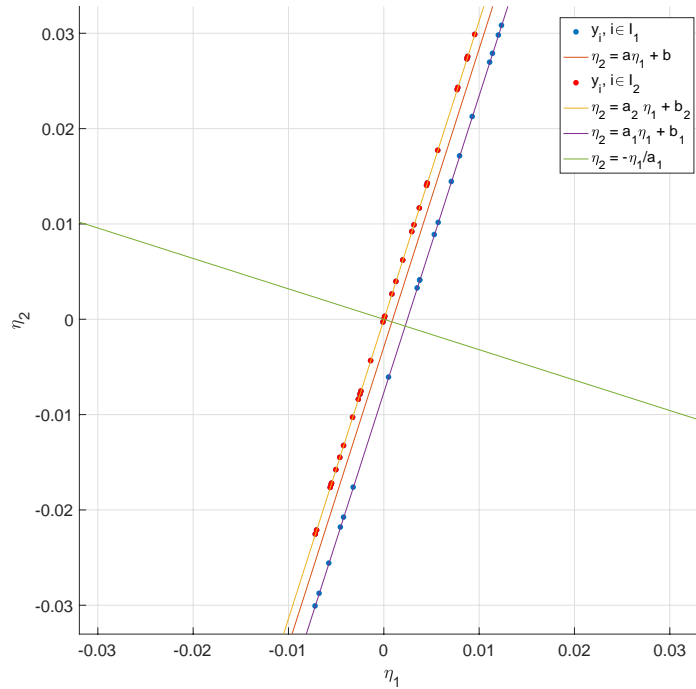


Figure 17: Estimating the thickness of the Lorenz attractor using linear least squares fits in a Poincare section.

References

- [1] R. Bartels and G. W. Stewart, *Solution of the matrix equation $AX + XB = C$* , Comm A.C.M., 15 (1972), 9, 820–826
- [2] R. E. Bellman, *Dynamic Programming*, Princeton University Press, Princeton, NJ, 1957
- [3] F. Bouchet and J. Reygner, *Generalisation of the Eyring-Kramers Transition Rate Formula to Irreversible Diffusion Processes*, Annales Henri Poincare, 17 (2016), 12, pp. 3499-3532
- [4] M. K. Cameron, *Finding the Quasipotential for Nongradient SDEs*, Physica D: Nonlinear Phenomena, 241 (2012), pp. 1532–1550
- [5] <https://www.math.umd.edu/~mariakc/software-and-datasets.html>
- [6] <https://github.com/mariakc/OLIM-for-Lorenz63>
- [7] A. Chacon and A. Vladimirovsky, *Fast two-scale methods for Eikonal equations*, SIAM J. on Scientific Computing 34, 2 (2012) A547–A578

- [8] Z. Chen, M. Freidlin, *Smoluchowski-Kramers approximation and exit problems*, Stoch. Dyn. 5 (2005), 4, pp. 569–585
- [9] Z. Chen, *Asymptotic Problems related to Smoluchowski-Kramers approximation*, Ph.D. Dissertation, UMD, 2006 <https://drum.lib.umd.edu/bitstream/handle/1903/3791/umi-umd-3634.pdf?sequence=1>
- [10] M. G. Crandall, P. L. Lions, *Viscosity solutions of Hamilton-Jacobi-Bellman equations*, Trans. Amer. Math. Soc. 277 (1983), pp. 1–43
- [11] D. Dahiya and M. Cameron, *Ordered Line Integral Methods for Computing the Quasi-potential*, J. Sci. Comput. (2017), (2017). <https://doi.org/10.1007/s10915-017-0590-9>
- [12] D. Dahiya and M. Cameron, *An Ordered Line Integral Method for Computing the Quasi-potential in the case of Variable Anisotropic Diffusion*, Physica D (2018) to appear, <https://doi.org/10.1016/j.physd.2018.07.002>, [arXiv:1806.05321](https://arxiv.org/abs/1806.05321)
- [13] S. V. Dudul, Prediction of a Lorenz chaotic attractor using two-layer perceptron neural network, Applied Soft Computing 5 (2005), 333–355
- [14] W. E, W. Ren, and E. Vanden-Eijnden, Minimum Action Method for the Study of Rare Events, Comm. Pure Appl. Math., **57**, 0001?0020 (2004)
- [15] M. I. Freidlin and A. D. Wentzell, *Random Perturbations of Dynamical Systems*, 3rd Ed, Springer-Verlag, Berlin Heidelberg, 2012.
- [16] C. Gissinger, A new deterministic model for chaotic reversals, Eur. Phys. J. B 85 (2012), 137–148
- [17] J. Guckenheimer and R. F. Williams, Structural stability of Lorenz attractors, Publications Mathematiques, I.H.E.S. 50 (1980) 73–100
- [18] F. Hamilton, T. Berry, and T. Sauer, Predicting chaotic time series with a partial model, Phys. Rev. E 92 (2015) 010902(R)
- [19] M. Heymann, E. Vanden-Eijnden, Pathways of maximum likelihood for rare events in non-equilibrium systems, application to nucleation in the presence of shear, Phys. Rev. Lett. **100**, 14, 140601 (2007)
- [20] M. Heymann, E. Vanden-Eijnden, The geometric minimum action method: a least action principle on the space of curves, Comm. Pure Appl. Math. **61**, 8, 1052–1117 (2008)
- [21] H. Ishii, *A simple direct proof of uniqueness for solutions of the Hamilton-Jacobi equations of eikonal type*, Proc. Amer. Math. Soc. 100 (1987), 2, pp. 247–251
- [22] J. L. Kaplan and J. A. Yorke, Preturbulence: A Regime Observed in a Fluid Flow Model of Lorenz, Commun. Math. Phys. 67 (1979), 93–108
- [23] Cheng Lv, Xiaoguang Li, Fangting Li, and Tiejun Li, Constructing the Energy Landscape for Genetic Switching System Driven by Intrinsic Noise, *PLOS One*, **9**, 2 (2014) [e88167](https://doi.org/10.1371/journal.pone.0088167)
- [24] E. N. Lorenz, *Deterministic Nonperiodic Flow*, J. Atmospheric Sci., 20 (1963), 2 pp. 130–141

- [25] J. Nocedal, S. J. Wright, Numerical Optimization, 2nd ed., Springer, USA, 2006.
- [26] D. Rand, The topological classification of Lorenz attractors, *Math. Proc. Camb. Phil. Soc.* 83 (1978) 451–460
- [27] B. Saltzman, Finite amplitude free convection as an initial value problem–I. *J. Atmos. Sci.*, 19 (1962), 329–341
- [28] J. .A. Sethian, A. Vladimirov, Ordered Upwind Methods for static Hamilton-Jacobi-Bellman equations, *Proc. Natl. Acad. Sci.* 98 (2001)11069–11074
- [29] J. A. Sethian, A. Vladimirov, Ordered Upwind Methods for static Hamilton-Jacobi-Bellman equations: theory and algorithms, *SIAM J. Numer. Anal.* 41, 1 (2003) 325–363
- [30] F. Sorrentino and E. Ott, Using synchronization of chaos to identify the dynamics of unknown systems, *Chaos* 19 (2009), 033108
- [31] C. Sparrow, *The Lorenz Equations. Bifurcations, Chaos, and Strange Attractors.* Springer-Verlag New York Inc. 1982
- [32] C. Sparrow, An introduction to the Lorenz Equations, *IEEE Transactions on Circuits and Systems, CAS-30*, 8 (1983), 533–542
- [33] S. H. Strogatz, *Nonlinear dynamics and Chaos*, 2nd edition, Westview Press, 2015
- [34] M. Tao, Hyperbolic periodic orbits in nongradient systems and small-noise-induced metastable transitions, *Physica D: Nonlinear Phenomena*, 363 (2018) pp. 1–17
- [35] D. Viswanath, The fractal property of the Lorenz attractor, *Physica D* 190 (2004), 115–128
- [36] R. F. Williams, The structure of Lorenz attractors, *Publications Mathématiques de l’IHÉS*, Volume 50 (1979), 73–99
- [37] J. A. Yorke and E. D. Yorke, Metastable chaos: Transition to sustained chaotic behavior in the Lorenz model, *J. Stat. Phys.*, 21 (1979), pp. 263–277
- [38] S. Yang, S. Potter, and M. Cameron, Computing the quasipotential for nongradient SDEs in 3D, *J. Comp. Phys.* 379 (2019) 325–350,
- [39] X. Zhou, W. Ren, Weiqing, W. E, Adaptive minimum action method for the study of rare events, *J. Chem. Phys.* 128, 104111 (2008)
- [40] X. Zhou and W. E, Study of noise-induced transitions in the Lorenz system using the minimum action method, *Commun. Math. Sci.*, 8, 2 (2010), 341–355